

Chapter 2

Finite-Difference Time-Domain Method

**Shinichi Sakamoto, Hideo Tsuru, Masahiro Toyoda
and Takumi Asakura**

Abstract In this chapter, analysis of sound and vibration using the Finite-Difference Time-Domain method (FDTD method) is illustrated. In Sect. 2.1, the fundamentals of the FDTD method are described. In the FDTD method, several error factors caused by discretization of sound field are pointed out. As methods to solve such problems, in Sect. 2.2, the compact finite difference is described in detail. The FDTD method can not only be applied to acoustic problem of air-borne sound, but also vibroacoustic problems such as a floor impact sound and a sound insulation problem through a wall structure. In Sect. 2.3, therefore, application of the FDTD method to vibroacoustic problems is focused on, and the theoretical background and its numerical formulation are described in detail.

Keywords Finite-difference time-domain (FDTD) method · Stability condition · FDTD(2, 4) method · Perfectly matched layer (PML) · Compact finite difference · Vibro-acoustic problem

S. Sakamoto (✉)

Institute of Industrial Science, The University of Tokyo, 4-6-1, Komaba, Meguro-ku,
Tokyo 153-8505, Japan
e-mail: sakamo@iis.u-tokyo.ac.jp

H. Tsuru

Nittobo Acoustic Engineering Co., Ltd., 1-21-10 Midori, Sumida-ku, Tokyo 130-0021, Japan
e-mail: tsuru@noe.co.jp

M. Toyoda

Faculty of Environmental and Urban Engineering, Kansai University, 3-3-35 Yamate-cho,
Suita-shi, Osaka 564-8680, Japan
e-mail: toyoda@kansai-u.ac.jp

T. Asakura

Institute of Technology, Shimizu Corporation, 3-4-17 Etchujima, Koto-ku, Tokyo 135-8530,
Japan
e-mail: t_asakura@shimz.co.jp

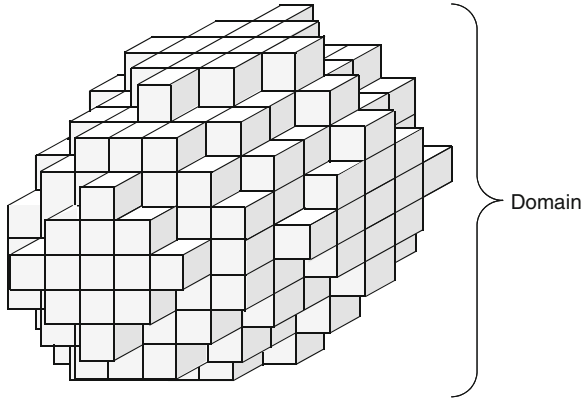


Fig. 2.1 Discretization of sound field

2.1 Fundamentals

2.1.1 Basic Equations

Sound propagation in the air is described by two kinds of differential equations, Euler's equation and the equation of continuity.

$$\rho \frac{\partial u}{\partial t} + \frac{\partial p}{\partial x} = 0, \quad (2.1)$$

$$\rho \frac{\partial v}{\partial t} + \frac{\partial p}{\partial y} = 0, \quad (2.2)$$

$$\rho \frac{\partial w}{\partial t} + \frac{\partial p}{\partial z} = 0, \quad (2.3)$$

$$\frac{\partial p}{\partial t} + \kappa \left(\frac{\partial u}{\partial x} + \frac{\partial v}{\partial y} + \frac{\partial w}{\partial z} \right) = 0, \quad (2.4)$$

where p , u , v , w are the sound pressure [Pa] and the particle velocities [m/s] in x , y , z directions, respectively, κ , ρ are volume elastic ratio [N/m²] and density [kg/m³] of the air, respectively.

By the Finite-Difference Time-Domain (FDTD) method, discrete physical acoustic quantities, sound pressure, and particle velocity are approximately updated based on finite difference schemes to which differential terms included in governed Euler's and continuity equations are substituted. For this purpose, in the first step, as shown in Fig. 2.1, sound field under test should be discretized in rectangular grids. Definition points of the sound pressure and the particle velocities are set at the

Fig. 2.2 Spatial definition points of sound pressure and particle velocities

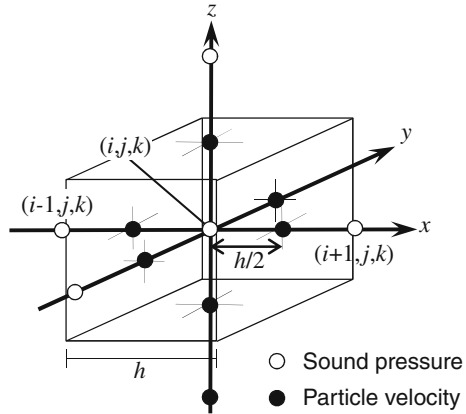
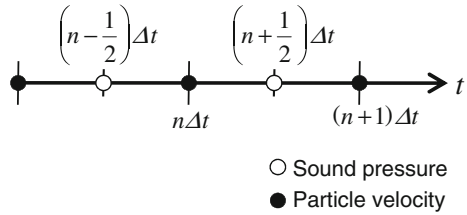


Fig. 2.3 Transient definition points of sound pressure and particle velocities



appropriate positions in the discretized grids, and the difference equations regarding the physical quantities are constructed. The difference equations based on the governed differential equations are called as “difference scheme”. The most representative difference scheme is “Yee algorithm” which is described in the following section [1].

In order to approximate a value of first-order derivative of Eqs. (2.1)–(2.4) by a central difference, definition points of sound pressure and particle velocities are set at a half grid apart from each other as shown in Fig. 2.2. Such a kind of grid system where different two kinds of physical quantities are defined at different points of which distance is equal to a half of the grid size is called the staggered grid system. In the same manner as the spatial grid their temporal definition points are also a half time step apart from each other, as shown in Fig. 2.3.

Suppose that a spatial grid size and a discrete time interval are h and Δt , and that a physical quantity q at spatial grid point $(x, y, z) = (ih, jh, kh)$ at a time $n\Delta t$ is described as $q_{i,j,k}^n$, then a sound pressure and particle velocities are expressed as, $p_{i,j,k}^{n+1/2}$, $u_{i+1/2,j,k}^n$, $v_{i,j+1/2,k}^n$, $w_{i,j,k+1/2}^n$. Using these expressions, differential terms in space and time appearing in Eqs. (2.1)–(2.4) become

$$\left. \frac{\partial u}{\partial t} \right|_{i+1/2,j,k}^{n+1/2} = \frac{u_{i+1/2,j,k}^{n+1} - u_{i+1/2,j,k}^n}{\Delta t}, \quad \left. \frac{\partial u}{\partial x} \right|_{i,j,k}^n = \frac{u_{i+1/2,j,k}^n - u_{i-1/2,j,k}^n}{h},$$

$$\frac{\partial p}{\partial t} \Big|_{i,j,k}^n = \frac{p_{i,j,k}^{n+1/2} - p_{i,j,k}^{n-1/2}}{\Delta t}, \quad \frac{\partial p}{\partial x} \Big|_{i+1/2,j,k}^{n+1/2} = \frac{p_{i+1,j,k}^{n+1/2} - p_{i,j,k}^{n+1/2}}{h}.$$

Substituting these into Eqs. (2.1)–(2.4) leads to following difference scheme:

$$u_{i+1/2,j,k}^{n+1} = u_{i+1/2,j,k}^n - \frac{\Delta t}{\rho h} \left(p_{i+1,j,k}^{n+1/2} - p_{i,j,k}^{n+1/2} \right), \quad (2.5)$$

$$v_{i,j+1/2,k}^{n+1} = v_{i,j+1/2,k}^n - \frac{\Delta t}{\rho h} \left(p_{i,j+1,k}^{n+1/2} - p_{i,j,k}^{n+1/2} \right), \quad (2.6)$$

$$w_{i,j,k+1/2}^{n+1} = w_{i,j,k+1/2}^n - \frac{\Delta t}{\rho h} \left(p_{i,j,k+1}^{n+1/2} - p_{i,j,k}^{n+1/2} \right), \quad (2.7)$$

$$\begin{aligned} p_{i,j,k}^{n+1/2} = & p_{i,j,k}^{n-1/2} - \frac{\kappa \Delta t}{h} \left[\left(u_{i+1/2,j,k}^n - u_{i-1/2,j,k}^n \right) \right. \\ & \left. + \left(v_{i,j+1/2,k}^n - v_{i,j-1/2,k}^n \right) + \left(w_{i,j,k+1/2}^n - w_{i,j,k-1/2}^n \right) \right]. \end{aligned} \quad (2.8)$$

From Eqs. (2.5)–(2.8), we can find features of the FDTD method.

- A future value of particle velocity in each direction (at a time step $n + 1$) is calculated by a known value of that (at a time step n) and a present values of sound pressure (at a time step $n + 1/2$).
- A future value of sound pressure (at a time step $n + 1/2$) is calculated by a known value of that (at a time step $n - 1/2$) and a present values of particle velocities in all directions (at a time step n).

Therefore, after an initial distribution of sound pressure and particle velocities, the distribution of sound pressure and particle velocity at the following time steps can be calculated successively.

2.1.2 Boundary Conditions

Reflection or absorption characteristics of boundaries are generally provided by surface acoustic impedance,

$$z_n = \frac{p}{u_n}, \quad (2.9)$$

where z_n is normal acoustic impedance and u_n is normal particle velocity.

In the simplest case where surface is perfectly reflective (rigid), the surface impedance becomes infinite and it is easy to adapt this condition to the FDTD scheme by making the particle velocity on the boundary nodes zero. On the other hand, for perfectly absorbing condition, the situation is not so simple. In a special case where

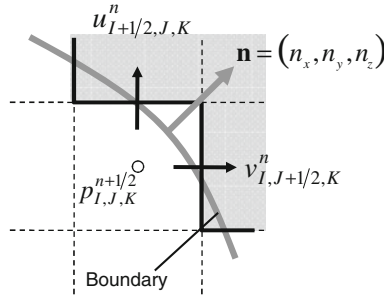


Fig. 2.4 Sound pressure and particle velocity near a boundary

a plane wave is incident perpendicularly to the absorbing boundary, the surface acoustic impedance becomes equal to the specific impedance of air. In such a case, $z_n = \rho c$ (c is speed of sound). However, if this absorbing condition is applied to a general case where the input sound is not plane wave but a cylindrical or spherical wave and its incidence angle is not perpendicular, theoretically there exists some reflection. More accurate perfectly absorbing boundary condition will be discussed in a latter part (Fig. 2.4).

In the Yee algorithm, both physical quantities of sound pressure p and particle velocity u, v, w are obtained successively in the calculation steps. Therefore, the surface acoustic impedance can be roughly approximated as [2],

$$u_{I+1/2,J,K}^{n+1} = \frac{p_{I,J,K}^{n+1/2}}{z_n} n_x, \quad (2.10)$$

$$v_{I,J+1/2,K}^{n+1} = \frac{p_{I,J,K}^{n+1/2}}{z_n} n_y, \quad (2.11)$$

$$w_{I,J,K+1/2}^{n+1} = \frac{p_{I,J,K}^{n+1/2}}{z_n} n_z, \quad (2.12)$$

where $\mathbf{n} = (n_x, n_y, n_z)$ is the normal vector of surface. Because the definition points of sound pressure and particle velocity are a half grid size apart from each other, note that this impedance is a rough approximation.

One of the most representative indices describing absorption characteristics of materials is the absorption coefficient α . The absorption coefficient, which is obtained on energy-base, is generally used in building acoustics, room acoustics, and environmental noise. The absorption coefficient is categorized into three kinds; normal incidence absorption coefficient α_0 , reverberation absorption coefficient $\bar{\alpha}$, and oblique incidence absorption coefficient α_θ . Among them, the normal incidence absorption coefficient α_0 is related to the normal acoustic impedance as

$$\alpha_0 = 1 - \left| \frac{z_n - \rho c}{z_n + \rho c} \right|. \quad (2.13)$$

Therefore, if normal incidence absorption coefficient of the material is known, normal acoustic impedance can be estimated as

$$z_n = \rho c \frac{1 + \sqrt{1 - \alpha_0}}{1 - \sqrt{1 - \alpha_0}}. \quad (2.14)$$

Acoustic impedance is generally treated in frequency domain and is expressed by complex values. By the above method, however, only real values can be treated for expressing the acoustic impedance because the FDTD method deals with physical quantities in real number, and such a treatment corresponds to a situation that acoustic impedance is a constant real value for all the frequency range under the calculation. In order to treat more complicated characteristics such that the acoustic impedance is dependent on frequency, another physical model is necessary. For such a complicated impedance model, some calculation models have been proposed. Sakamoto has proposed the mechanical substitution model in which the acoustic boundary surface has been substituted by an equivalent mechanical model being composed of mass, spring, and resistance [3]. In order to treat more general impedance characteristics, D. M. Sullivan has used Z transform to deal with a linear system in sound reflection by boundary surface [4]. Escolano has used digital signal processing, in which an acoustic admittance was modeled with IIR or FIR filters [5]. For a case where homogeneous porous materials such as glass fibrous board or urethane foam are used as a surface absorption material, Suzuki has proposed a calculation method by which the inner space of the material was digitized and sound propagation was obtained based on the Rayleigh model [6].

2.1.3 FDTD(2, 4) Method

In the Yee algorithm, central difference using two reference points secures second-order accuracy. In order to raise the accuracy, various efforts have been made. In this section, as the simplest method for the implementation, FDTD(2, 4) method [7, 8] is introduced. FDTD(2, 4) means the second-order accuracy in time and the fourth-order accuracy in space. The spatial accuracy is raised by adopting the fourth-order scheme using four points central difference. For temporal derivative, however, the method remains to use two points central difference with the second-order accuracy in order to avoid increase of computational memory usage.

The difference scheme with fourth-order accuracy using four reference points is deduced from Taylor expansion of a function. Values of a function f at points $x \pm h/2$ and $x \pm 3h/2$, $f(x \pm h/2)$ and $f(x \pm 3h/2)$, are expressed as follows, by using the Taylor expansion around x .

$$f\left(x + \frac{h}{2}\right) = f(x) + \frac{1}{2}f^{(1)}(x)h + \frac{1}{8}f^{(2)}(x)h^2 + \frac{1}{48}f^{(3)}(x)h^3 + \frac{1}{384}f^{(4)}(x)h^4 + \dots, \quad (2.15)$$

$$f\left(x - \frac{h}{2}\right) = f(x) - \frac{1}{2}f^{(1)}(x)h + \frac{1}{8}f^{(2)}(x)h^2 - \frac{1}{48}f^{(3)}(x)h^3 + \frac{1}{384}f^{(4)}(x)h^4 + \dots, \quad (2.16)$$

$$f\left(x + \frac{3h}{2}\right) = f(x) + \frac{3}{2}f^{(1)}(x)h + \frac{9}{8}f^{(2)}(x)h^2 + \frac{9}{16}f^{(3)}(x)h^3 + \frac{27}{128}f^{(4)}(x)h^4 + \dots, \quad (2.17)$$

$$f\left(x - \frac{3h}{2}\right) = f(x) - \frac{3}{2}f^{(1)}(x)h + \frac{9}{8}f^{(2)}(x)h^2 - \frac{9}{16}f^{(3)}(x)h^3 + \frac{27}{128}f^{(4)}(x)h^4 + \dots. \quad (2.18)$$

In order to deduce $\frac{\partial f}{\partial x}$ from the above four equations, let us calculate $\{(2.15) - (2.16)\} \times 27 - \{(2.17) - (2.18)\}$, then

$$f^{(1)}(x) = \frac{-f(x + 3h/2) + 27f(x + h/2) - 27f(x - h/2) + f(x - 3h/2)}{24h} + \epsilon, \quad (2.19)$$

where ϵ is an error term and it becomes fourth-order accurate as

$$\epsilon = \frac{3}{640}f^{(5)}(x)h^4. \quad (2.20)$$

An FDTD scheme where temporal and spatial derivatives are approximated in the second-order and fourth-order accuracy, respectively, is called the FDTD(2, 4) method, and the schemes are expressed as

$$u_{i+1/2,j,k}^{n+1} = u_{i+1/2,j,k}^n - \frac{\Delta t}{\rho h} \sum_{m=0}^1 C_m \left(p_{i+m,j,k}^{n+1/2} - p_{i-m,j,k}^{n+1/2} \right), \quad (2.21)$$

$$v_{i,j+1/2,k}^{n+1} = v_{i,j+1/2,k}^n - \frac{\Delta t}{\rho h} \sum_{m=0}^1 C_m \left(p_{i,j+m,k}^{n+1/2} - p_{i,j-m,k}^{n+1/2} \right), \quad (2.22)$$

$$w_{i,j,k+1/2}^{n+1} = w_{i,j,k+1/2}^n - \frac{\Delta t}{\rho h} \sum_{m=0}^1 C_m \left(p_{i,j,k+m}^{n+1/2} - p_{i,j,k-m}^{n+1/2} \right), \quad (2.23)$$

$$\begin{aligned} p_{i,j,k}^{n+1/2} = & p_{i,j,k}^{n-1/2} - \frac{\kappa \Delta t}{h} \left[\sum_{m=0}^1 C_m \left(u_{i+1/2,j,k}^n - u_{i-1/2,j,k}^n \right) \right. \\ & + \sum_{m=0}^1 C_m \left(v_{i,j+1/2,k}^n - v_{i,j-1/2,k}^n \right) \\ & \left. + \sum_{m=0}^1 C_m \left(w_{i,j,k+1/2}^n - w_{i,j,k-1/2}^n \right) \right]. \end{aligned} \quad (2.24)$$

where $C_0 = \frac{9}{8}$ and $C_1 = \frac{1}{24}$.

2.1.4 Stability and Dispersion Error

Whereas the FDTD method is easy to be implemented, the method has a sensitive nature in which a solution unexpectedly diverges or fluctuates depending on a calculation condition. Such natures as unexpected divergence and fluctuation are caused by violation of stability condition and dispersion error, respectively. Among them, the stability condition is simpler and it is provided by relationship between discrete time step Δt and spatial grid size h as,

$$\Delta t \leq \frac{h}{c} \quad (1 \text{ dimension}), \quad (2.25)$$

$$\Delta t \leq \frac{h}{\sqrt{2}c} \quad (2 \text{ dimension}), \quad (2.26)$$

$$\Delta t \leq \frac{h}{\sqrt{3}c} \quad (3 \text{ dimension}), \quad (2.27)$$

for the Yee algorithm using temporal second-order. This condition is called the Courant condition. As shown in the above equation, for appropriate parameter setting, a discrete time step is proportional to a spatial grid size. Therefore, more precise modeling or raising upper limit frequency by shortening a spatial grid size leads to a temporal high resolution. In this section, this stability condition is theoretically explained.

A simple technique for analyzing the stability and the dispersive phase error of a finite difference scheme has been given by Von Neumann and Richtmyer [9]. Consider a plane wave with wave number k traveling in the (θ, φ) direction in polar coordinates shown in Fig. 2.5. The sound pressure at a point (x, y, z) with a wave number k ($= \omega/c$) and an amplitude of 1 is assumed to be

$$p_0(x, y, z, t) = e^{jk_x x} e^{jk_y y} e^{jk_z z} e^{-j\omega t}, \quad (2.28)$$

where k_x, k_y, k_z are directional component of the wave number k and they are expressed as $k_x = k \sin \varphi \cos \theta, k_y = k \sin \varphi \sin \theta, k_z = k \cos \varphi$.

Sound pressure and particle velocity at their definition points on the staggered grid system are expressed as

$$u_{i+1/2,j,k}^n = u_0 Z^n \cdot e^{jk_x(i+1/2)h} e^{jk_y(jh)} e^{jk_z(kh)}, \quad (2.29)$$

$$p_{i,j,k}^{n+1/2} = p_0 Z^{n+1/2} \cdot e^{jk_x(ih)} e^{jk_y(jh)} e^{jk_z(kh)}, \quad (2.30)$$

where u_0, v_0, w_0, p_0 are initial values, Z is a complex amplification ratio per time step. Substituting the above expressions into Eqs. (2.5)–(2.8) leads to

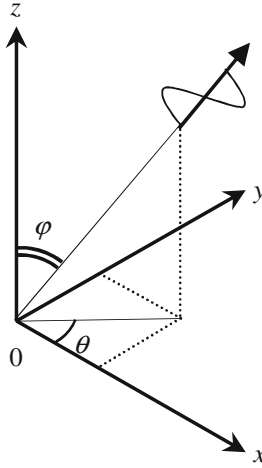


Fig. 2.5 Traveling direction of a plane wave

$$u_0 \left(Z^{\frac{1}{2}} - Z^{-\frac{1}{2}} \right) - \frac{\Delta t}{\rho h} \cdot 2j p_0 \sin \frac{k_x h}{2} = 0, \quad (2.31)$$

$$v_0 \left(Z^{\frac{1}{2}} - Z^{-\frac{1}{2}} \right) - \frac{\Delta t}{\rho h} \cdot 2j p_0 \sin \frac{k_y h}{2} = 0, \quad (2.32)$$

$$w_0 \left(Z^{\frac{1}{2}} - Z^{-\frac{1}{2}} \right) - \frac{\Delta t}{\rho h} \cdot 2j p_0 \sin \frac{k_z h}{2} = 0, \quad (2.33)$$

$$p_0 \left(Z^{\frac{1}{2}} - Z^{-\frac{1}{2}} \right) - \frac{\Delta t}{\rho h} \left(2j \sin \frac{k_x h}{2} u_0 + 2j \sin \frac{k_y h}{2} v_0 + 2j \sin \frac{k_z h}{2} w_0 \right) = 0. \quad (2.34)$$

In a matrix form of Eqs. (2.31)–(2.34),

$$\begin{bmatrix} Z^{\frac{1}{2}} - Z^{-\frac{1}{2}} & 0 & 0 & -\frac{\Delta t}{\rho h} 2j \sin \frac{k_x h}{2} \\ 0 & Z^{\frac{1}{2}} - Z^{-\frac{1}{2}} & 0 & -\frac{\Delta t}{\rho h} 2j \sin \frac{k_y h}{2} \\ 0 & 0 & Z^{\frac{1}{2}} - Z^{-\frac{1}{2}} & -\frac{\Delta t}{\rho h} 2j \sin \frac{k_z h}{2} \\ -\frac{\kappa \Delta t}{h} 2j \sin \frac{k_x h}{2} & -\frac{\kappa \Delta t}{h} 2j \sin \frac{k_y h}{2} & -\frac{\kappa \Delta t}{h} 2j \sin \frac{k_z h}{2} & Z^{\frac{1}{2}} - Z^{-\frac{1}{2}} \end{bmatrix} \begin{bmatrix} u_0 \\ v_0 \\ w_0 \\ p_0 \end{bmatrix} = \begin{bmatrix} 0 \\ 0 \\ 0 \\ 0 \end{bmatrix}. \quad (2.35)$$

A value of determinant of the 4×4 matrix which appears in Eq. (2.35) should be zero, in order that the vector $[u_0 \ v_0 \ w_0 \ p_0]^T$ is non-zero vector. This condition leads the following equation regarding the complex amplification ratio Z as follows:

$$Z^2 - 2AZ + 1 = 0, \quad (2.36)$$

$$A = 1 - 2 \left(\frac{c \Delta t}{h} \right)^2 \left(\sin^2 \frac{k_x h}{2} + \sin^2 \frac{k_y h}{2} + \sin^2 \frac{k_z h}{2} \right). \quad (2.37)$$

A solution of Eq. (2.36) is

$$Z = \begin{cases} A \pm \sqrt{A^2 - 1} & (A < -1) \\ A \pm j\sqrt{1 - A^2} & (-1 \leq A \leq 1). \end{cases} \quad (2.38)$$

If an absolute value of Z in Eq. (2.38) is greater than 1, the solution increases with advance of time steps and diverges at last. Accordingly, $-1 \leq A \leq 1$ is a necessary condition for the solution being stable. Actually in this case, $|Z|$ is equal to 1 and $\arg Z = \arctan A/\sqrt{1 - A^2}$. The fact means that the wave amplitude does not change and the phase of the wave shifts with the progress of time steps. Then, Eq. (2.37) leads to

$$\sin^2 \frac{k_x h}{2} + \sin^2 \frac{k_y h}{2} + \sin^2 \frac{k_z h}{2} \leq \left(\frac{h}{c \Delta t} \right)^2. \quad (2.39)$$

For arbitrary k ,

$$\Delta t \leq \frac{h}{\sqrt{3}c} \quad (2.40)$$

can be obtained because $\sin(k_x h/2) \leq 1$, $\sin(k_y h/2) \leq 1$, $\sin(k_z h/2) \leq 1$. A value of A is dependent on the wave number k (see Eq. (2.37)) and therefore the degree of the numerical phase shift is also dependent on the wave number k . This error of phase shift owing to frequency is called dispersion error. Figure 2.6 shows an example of a pulse propagation with dispersion error. At a center point in a cubic room of $201 h \times 201 h \times 201 h$, a pulse source is emitted and its pulse propagation is detected at a corner point. Comparing with a theoretical solution reveals that dispersion error accumulates in 10,000 time steps to raise numerical fluctuations. The influence of dispersion error on calculation results of sound propagation becomes severer as size of sound field under test is larger. Therefore, various efforts have been made to reduce such dispersion error heretofore as shown in the following section.

2.1.5 Absorbing Boundary Condition

When the FDTD method, which is categorized in a domain-type is applied to a free field, a special treatment is required to reduce reflection sound from field terminations. As a concept of absorbing boundary condition (ABC), we can choose two kinds; Differential-based Absorbing Boundary Condition (D-ABC) and Material-based Absorbing Boundary Condition (M-ABC). The former deals with progressive and regressive waves at a terminating surface, and the latter absorbs sound energy

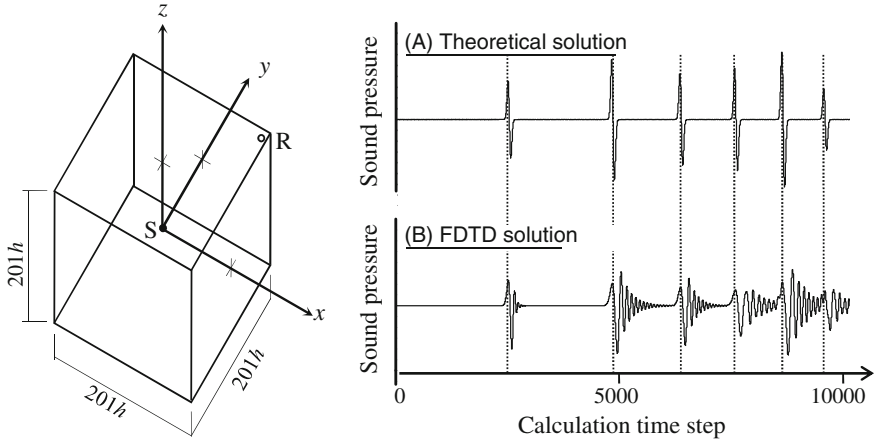


Fig. 2.6 Numerical fluctuation caused by dispersion error appearing in a numerical result

inside a numerically lossy media with sufficient thickness installed along surrounding boundary. As representative D-ABC and M-ABC, hereafter, the Mur ABC and the perfectly matched layer (PML), respectively, will be introduced.

2.1.5.1 Mur Absorbing Boundary Condition

The simplest and most commonly used grid truncation technique for open-field FDTD modeling is the Mur ABC [10]. The Mur ABC is based on a concept in which only progressive wave outgoing to an absorbing boundary exits and there exists no regressive wave inbound sound field at truncation mesh of the boundary. Now, let us consider one-dimensional wave equation in x -direction regarding x -component of particle velocity.

$$\left(\frac{\partial^2}{\partial x^2} - \frac{1}{c^2} \frac{\partial^2}{\partial t^2} \right) u = 0. \quad (2.41)$$

The above second-order differential equation is transformed as

$$\frac{\partial u}{\partial x} - \frac{1}{c} \frac{\partial u}{\partial t} = 0, \quad (2.42)$$

$$\frac{\partial u}{\partial x} + \frac{1}{c} \frac{\partial u}{\partial t} = 0, \quad (2.43)$$

then the solutions of Eqs. (??)–(2.43) mean a progressive and a regressive plane waves, respectively. For example, in the case of Fig. 2.7, in which absorbing boundary

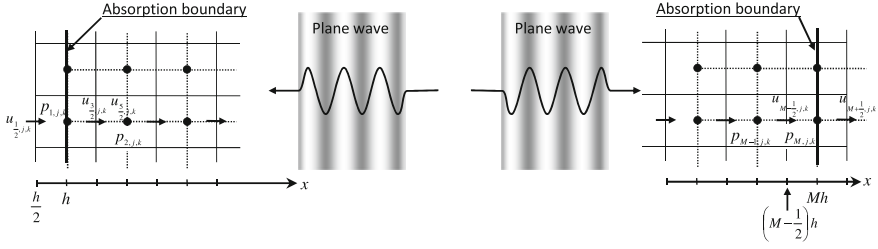


Fig. 2.7 A plane wave incidence to an absorbing boundary

is set at $x = h/2$, there exists a progressive wave in negative x -direction, Eq. (2.43) should be applied at $x = h/2$. With adopting the grid system to the Yee's staggered system, discretization of Eq. (??) at a time step $(n + 1/2)\Delta t$ by,

$$\left. \frac{\partial u}{\partial x} \right|_{i,j,k}^{n+\frac{1}{2}} = \frac{1}{c} \left. \frac{\partial u}{\partial t} \right|_{i,j,k}^{n+\frac{1}{2}}, \quad (2.44)$$

leads,

$$\begin{aligned} & \frac{(u_{3/2,j,k}^{n+1} + u_{3/2,j,k}^n) - (u_{1/2,j,k}^{n+1} + u_{1/2,j,k}^n)}{2h} \\ &= \frac{(u_{3/2,j,k}^{n+1} + u_{1/2,j,k}^{n+1}) - (u_{3/2,j,k}^n + u_{1/2,j,k}^n)}{2c\Delta t}. \end{aligned} \quad (2.45)$$

By arranging Eq. (2.45) regarding a particle velocity at a truncation boundary grid, the Mur ABC is obtained as

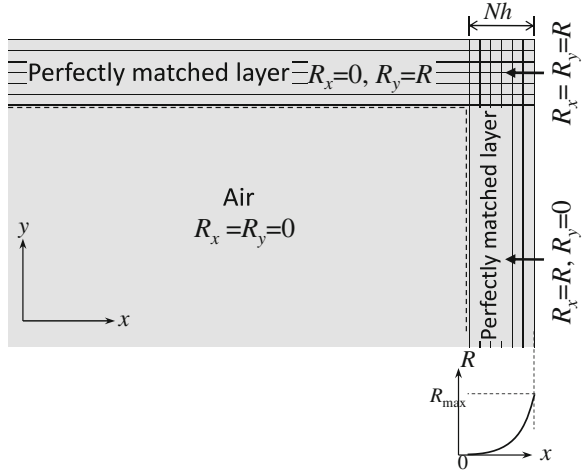
$$u_{1/2,j,k}^{n+1} = u_{3/2,j,k}^n - \frac{c\Delta t - h}{c\Delta t + h} (u_{1/2,j,k}^n - u_{3/2,j,k}^{n+1}). \quad (2.46)$$

Note that the above formulation is premised that a plane wave is normally incident on the absorbing boundary. Therefore, its accuracy deteriorates for an oblique incidence or a spherical wave incidence.

2.1.5.2 Perfectly Matched Layer

By D-ABC, a nonreflective boundary is approximated by a concept that only outward wave through a truncation boundary propagates and there exists no inward wave propagating to the problem region.

On the other hand, by M-ABC, sound wave penetrates into a lossy media with a certain thickness, which is adjacent to a problem region, and the sound energy vanishes in the lossy media, and consequently, reflecting sound from the truncation boundary is decreased. The PML developed by Berenger [11], which utilizes such a sound absorbing process, is the most flexible and efficient M-ABC.

Fig. 2.8 Setting of PML

The following equations to which resistance terms specified by R_x , R_y and R_z are introduced are basic equations of the acoustic PML.

$$\rho \frac{\partial u}{\partial t} + R_x u + \frac{\partial p}{\partial x} = 0, \quad \frac{\partial p_x}{\partial t} + \frac{R_x}{\rho} p_x + \kappa \frac{\partial u}{\partial x} = 0, \quad (2.47)$$

$$\rho \frac{\partial v}{\partial t} + R_y v + \frac{\partial p}{\partial y} = 0, \quad \frac{\partial p_y}{\partial t} + \frac{R_y}{\rho} p_y + \kappa \frac{\partial v}{\partial y} = 0, \quad (2.48)$$

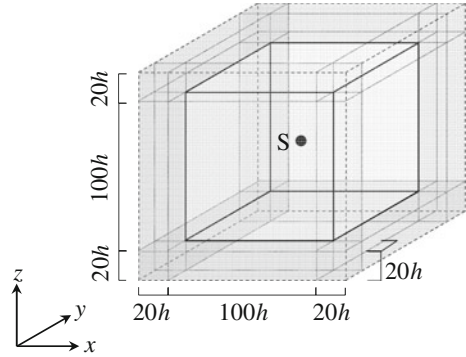
$$\rho \frac{\partial w}{\partial t} + R_z w + \frac{\partial p}{\partial z} = 0, \quad \frac{\partial p_z}{\partial t} + \frac{R_z}{\rho} p_z + \kappa \frac{\partial w}{\partial z} = 0, \quad (2.49)$$

$$p = p_x + p_y + p_z. \quad (2.50)$$

As shown in Eqs. (2.1)–(2.4) and Eqs. (2.47)–(2.50), governed equations in the PML are different from those in the air, and therefore, discontinuity of sound propagation media might cause sound reflection. The PML, however, contrives treatment of resistance terms so that the specific impedance of the PML media becomes equal to that of the air, and consequently, the impedance matching ensures no reflection from the interface-surface between the air and the PML media. As a special case, $R_x = R_y = R_z = 0$ leads Eqs. (2.1)–(2.4), which describe sound propagation in the air.

Figure 2.8 shows how to set PML layer for two-dimensional field. In the figure, upper PML diminishes a wave going in positive y -direction by introducing R_y as a positive value. Resistance term in x -direction does not contribute to reduction in the wave, so R_x is made to be zero. On the other hand, the right-hand side layer which weakens a wave going in positive x -direction has a positive value as a parameter of R_x and zero value as that of R_y .

Fig. 2.9 Setting of a cubic sound field modeling a free field



When medium changes between two layers, the discontinuity of the medium results in a reflection from the interface, and the reflection may cause a numerical error. In the PML calculation, such a numerical error is usually reduced by smooth change of value of R in the PM layer. When total number of grids of a PM layer is N , for example, the value of R is given with a function of distance from the interface as

$$R(ih) = R_{\max} \left(\frac{ih}{Nh} \right)^m, \quad (2.51)$$

where m is a constant determining spatial distribution pattern of R . As is shown in the equation, when $i = 0$, R is made to be zero and a sound wave smoothly penetrates through the PM layer. As i is increased, the value of R becomes rapidly larger. The PML calculation gradually decreases the amplitude of the traveling wave in the lossy media with a certain depth, and therefore the calculation method is robust for the incidence angle than D-ABC. In order to see a difference in absorption characteristics between D-ABC and M-ABC, transition of sound pressure distribution for a cubic sound field shown in Fig. 2.9 with perfect absorption on all six walls was calculated for the following two cases—1: Mur-ABC, 2: PML with $N = 20$. Comparison of the calculation results are shown in Fig. 2.10. The figure shows every $64\Delta t$ snapshot of sound pressure distribution on a center x - y plane where a sound source exists. In a calculation result of Mur-ABC, slight reflection is seen, especially, amplitudes of the reflection from corners are larger than those from centers of boundary surfaces. On the other hand, in the case of the PML, penetrating wave gradually diminishes in the absorbing layer. As is seen in the figure, highly efficient perfectly absorbing boundary condition is realized by using the PML, but it should be noted that computational load becomes much larger than that of D-ABC from viewpoints of both of computer storage necessity and computational time.

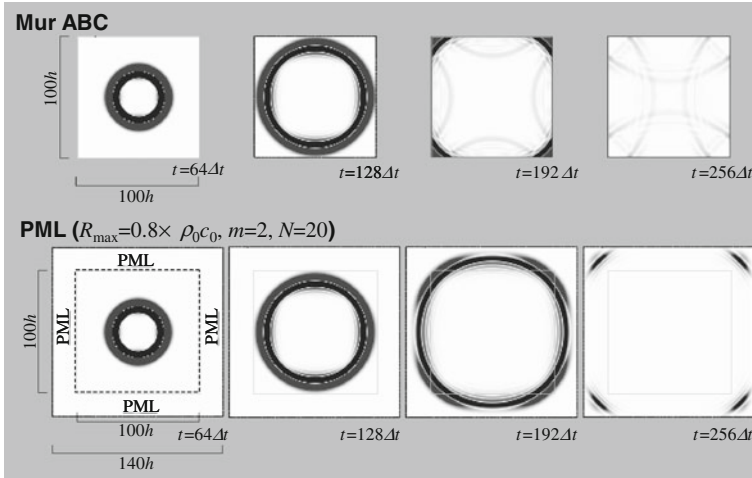


Fig. 2.10 Snapshots of sound pressure distribution in horizontal plane which includes a source

2.2 Techniques for High Accuracy

When accurate values of differentiations by finite difference are required, a grid spacing should be small compared to a typical wave length in the problem. Therefore, for a high frequency problem, the grid spacing has to be small and the degree of freedom amounts to a huge value. In order to resolve this problem, a higher order or a compact difference method can be applied. Since the time integration must be fulfilled after evaluating spatial differentiations, the accuracy of the time marching procedure must be maintained. In order to carry out the time integration accurately, a symplectic integration can be applied in the acoustic problem.

2.2.1 Compact Finite Difference

In the acoustic FDTD simulation, the variables are usually defined on a staggered grid. On the staggered grid the scalar variables (pressure, mass density, sound speed, etc.) are stored in the cell centers of the control volumes, whereas the particle velocities are located at the cell faces.

Since small grid spacing compared to the typical wavelength is required to obtain an accurate differential value when a conventional finite difference scheme is used, the grid spacing has to be small and the degree of freedom becomes huge for high frequency problems. In order to resolve this problem, a higher order explicit or a compact finite difference has been applied [12]. In the compact finite difference, differential values are coupled and fewer grid points are required for constructing the difference formula than the explicit finite difference. The differential value is

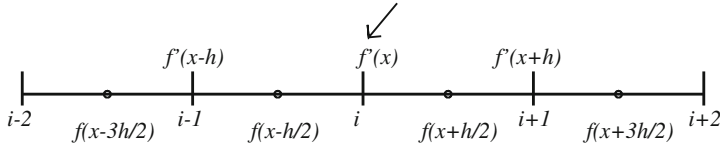


Fig. 2.11 Evaluation points of differential and difference values on the uniform staggered grid

determined by the linear coupled equations whose coefficient matrix is a band matrix. A fast algorithm can be applied to solve the linear equations with a tridiagonal coefficient matrix.

The numerical dispersion of a compact finite difference on a uniform staggered grid can be minimized by adjusting the coefficients. The evaluation points of the differentiation and the difference values on staggered the uniform staggered grid are illustrated in Fig. 2.11. Introducing a parameter α , we consider a compact finite difference on a grid with a uniform spacing h ,

$$\alpha f'_{i+1} + f'_i + \alpha f'_{i-1} = b \frac{f_{i+3/2} - f_{i-3/2}}{3h} + a \frac{f_{i+1/2} - f_{i-1/2}}{h} + \epsilon. \quad (2.52)$$

Here, the coefficients a , b and the error term ϵ are related to α by

$$\begin{aligned} a &= \frac{3}{8}(3 - 2\alpha), \quad b = \frac{22\alpha - 1}{8}, \\ \epsilon &= \frac{9 - 62\alpha}{1920} h^4 f^{(5)} + O(h^6). \end{aligned} \quad (2.53)$$

The differential values are calculated by solving a linear equation with a tridiagonal coefficient matrix. When $\alpha = 1/22$, the coefficient b vanishes and the compact finite difference is represented by a least number of grid points. Thus, this case is convenient for the simulation of the wave propagation in a region of complex configuration. When $\alpha = 9/62$, the fourth-order error term in ϵ vanishes and the difference equation becomes sixth order. We evaluate effective wave number k' which is defined by the function $f(x) = \sin(kx)$ and its first-order differentiation $k' \cos(kx)$ evaluated by a finite difference. The grid wave number $w = hk$ and the effective grid wave number $w' = hk'$ are defined by the grid spacing h . For example, $w = \pi/2$ means that 4 grid points exist per one wavelength (4 PPW: point per wavelength). By the second-order explicit finite difference on the staggered grid, the effective grid wave number becomes $w' = 2 \sin(w/2)$. This deviates from the exact value when the grid wave number is not very small. On the other hand, for the compact finite difference with α , we obtain

$$w'(w, \alpha) = \frac{2a \sin(\frac{w}{2}) + \frac{2}{3}b \sin(\frac{3w}{2})}{1 + 2\alpha \cos(w)}. \quad (2.54)$$

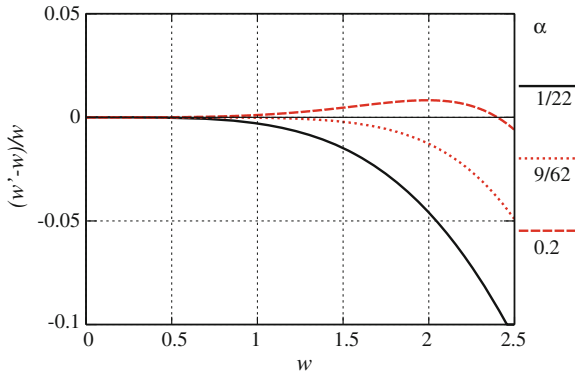


Fig. 2.12 Effective grid wave number error for various α

The exact value is $w = w'$ and the deviation from the exact value causes numerical dispersion error. Some properties of w' , i.e.,

$$w'(0, \alpha) = 0, w'(\pi, \alpha) = \frac{7 - 10\alpha}{3(1 - 2\alpha)}, \quad (2.55)$$

$$w'(\pi, \alpha) < \pi, \text{ when } \alpha < \frac{3\pi - 7}{6\pi - 10} \approx 0.27, \quad (2.56)$$

are derived. Therefore, when α is less than 0.27, there exists a point w_1 ($0 < w_1 < \pi$) where $w = w'$, i.e.,

$$w'(w_1, \alpha) = w_1. \quad (2.57)$$

Furthermore, $w' > w$ holds in the interval $(0, w_1)$, and $w' < w$ in (w_1, π) . If $\alpha > 9/62$ then $w'(w, \alpha)$ is larger than the exact grid wave number in the vicinity of $w = 0$. General tendency is that, when α is small, the effective wave number becomes less than the theoretical value even if the PPW is not so small. On the other hand, when α is large, the effective wave number can approximate the theoretical value well up to the region of short wavelength ($w \geq \pi/2$). The effective grid wave number error is shown in Fig. 2.12. For w_1 in $(0, \pi)$, w_1 and α are related by

$$\alpha = \frac{27 \sin(\frac{1}{2}w_1) - \sin(\frac{3}{2}w_1) - 12w_1}{18 \sin(\frac{1}{2}w_1) - 22 \sin(\frac{3}{2}w_1) + 24w_1 \cos(w_1)}. \quad (2.58)$$

Therefore, adjusting α can improve the accuracy of the finite difference in a given interval of w . In order to optimize α , we have adopted the following strategy. First, we set the maximum wave number w_0 to be analyzed. Next, α is determined so that the maximum absolute value of relative error in the interval $(0, w_0)$ is minimized.

The maximum absolute value of relative error in the interval of $(0, w_0)$ is plotted in Fig. 2.13 where the abscissa means α . We see that the minimization is attained

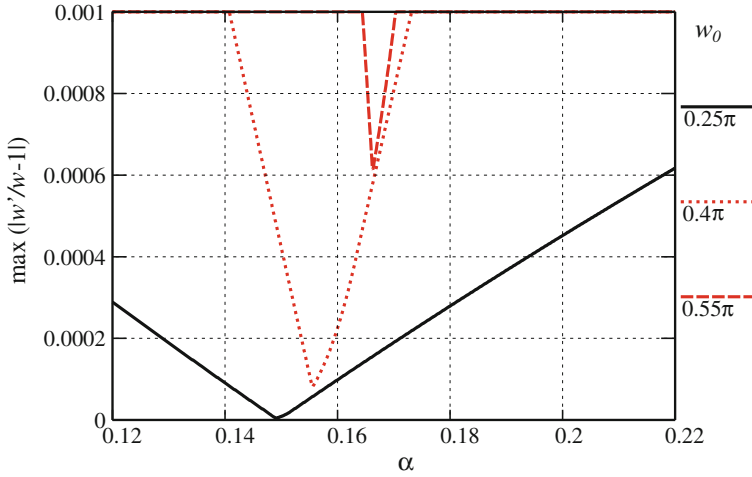


Fig. 2.13 Maximum absolute value of relative error for the various intervals of $(0, w_0)$. The abscissa represents α . The minimization of the maximum absolute value of error is realized by adjusting α

Table 2.1 Maximum wave number w_0 , optimized α and maximum relative error. The optimization of α reduces the maximum absolute value of relative error below 10^{-5}

w_0	Point per wave length (PPW)	Optimized α	Maximum relative error
0.25π	8	0.14905	4.5×10^{-6}
0.3π	6.67	0.1508	1.4×10^{-5}
0.4π	5	0.15555	8.1×10^{-5}
0.5π	4	0.1621	3.3×10^{-4}
0.55π	3.64	0.16625	6.1×10^{-4}

by adjusting the parameter α . In Table 2.1, maximum wave number, optimized α , and maximum absolute value of relative error are shown. The maximum absolute value of relative error is reduced even when the PPW is not so large. This estimation has been done using a local property of coefficients, only. However, in the compact finite difference, the differential values are coupled with those of the adjacent points. Therefore, the differential value computed by the compact scheme is influenced by those of neighboring grid points. When the interval is finite and non periodic, the boundary difference scheme must be also considered.

There are two types of boundary differences in the staggered grid. The first type is that the evaluation point of the differential value is outside of the interval of difference value estimation. This type corresponds to the boundary difference of the pressure which is utilized for time evolution of the velocity. However, this differential value need not to be evaluated for a rigid boundary condition in the acoustic problem because the velocity on the rigid boundary is always zero. The evaluation points of

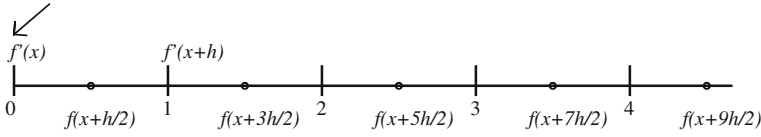


Fig. 2.14 Evaluation points of differential and difference values on boundary grid

the differentiation and the difference values on the boundary grid are illustrated in Fig. 2.14. The compact finite difference formula on the boundary is

$$f'_0 + \alpha_b f'_1 = \frac{1}{h} (a_b f_{1/2} + b_b f_{3/2} + c_b f_{5/2} + d_b f_{7/2} + e_b f_{9/2}) + \epsilon. \quad (2.59)$$

Here, coefficients are related to α_b by

$$\begin{aligned} a_b &= -\frac{22\alpha_b + 93}{24}, b_b = \frac{17\alpha_b + 229}{24}, c_b = \frac{3\alpha_b - 75}{8}, \\ d_b &= \frac{-5\alpha_b + 111}{24}, e_b = \frac{\alpha_b - 22}{24}, \end{aligned} \quad (2.60)$$

and ϵ is the error term,

$$\epsilon = \left(\frac{71\alpha_b}{1920} - \frac{563}{640} \right) h^4 f^{(5)} + O(h^5). \quad (2.61)$$

For a function $f(x) = \cos(kx) + j \sin(kx)$, its differential value approximated by a finite difference, $f'(x) = jk'[\cos(kx) + \sin(kx)]$ is evaluated. Using grid wave number $w = hk$, w' is given by

$$jw' = \frac{a_b e^{jw/2} + b_b e^{j3w/2} + c_b e^{j5w/2} + d_b e^{j7w/2} + e_b e^{j9w/2}}{1 + \alpha_b e^{jw}}. \quad (2.62)$$

Global consideration must be executed because the differential values on the inner and boundary grid points are coupled. As an attempt to investigate the nonlocal property of the compact finite difference scheme, a spatial distribution of the amplitude error in a whole interval of a given grid is calculated by solving a system of linear equations with the tridiagonal coefficient matrix. The spatial distribution of the amplitude error in the interval with $n = 60$ grid points is demonstrated in Fig. 2.15. The wavelength is set to be 6 grid spacing (6 PPW). For the estimation of the compact difference, α of inner interval ($2 \leq i \leq n - 2$) is set to be the optimum value for the frequency range below 6 PPW. For the evaluation of differentiation on the grid points next to the boundary ($i = 1, n - 1$), α is set to be $1/22$. At the grid points on both boundaries, α_b is set to be 21.88. The error is the largest on each boundary grid point $i = 0, n$. We evaluate the maximum absolute value of amplitude error on the boundary grid

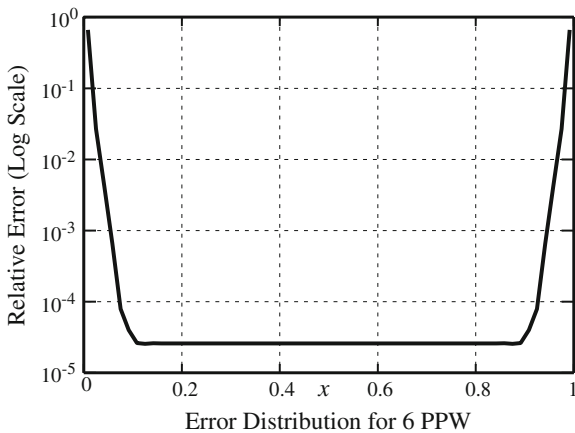


Fig. 2.15 Distribution of the absolute value of relative amplitude error on the grid with 60 points. The grid wave number is set to be $\pi/3$ (6 PPW)

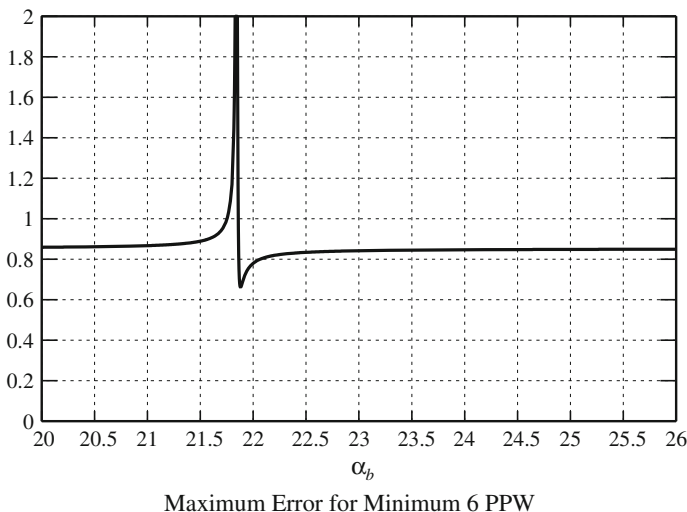


Fig. 2.16 Maximum absolute value of amplitude error versus α_b below upper bound frequency

point in the frequency range to be considered. The dependence of the error on α_b is demonstrated in Fig. 2.16. The absolute value of the relative error is not small in this case. Moreover, when α_b is near 22, the inverse of $1/22$, the maximum amplitude error diverges. Thus, we can conclude that the optimization may not work well for this type of boundary difference when the value of PPW is not large.

The second type of boundary difference is that the evaluation point of differentiation lies between grid points for difference estimation. This case corresponds to the boundary difference of velocity in acoustic FDTD which is utilized

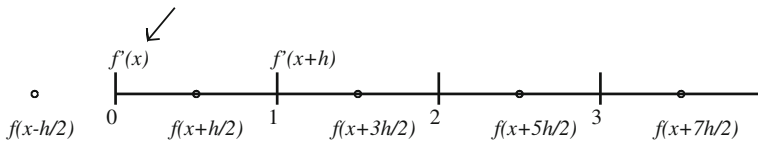


Fig. 2.17 Evaluation points of differential and difference values on boundary grid

for time evolution of the pressure at the boundary cell. The evaluation points of the differentiation and the difference values on the boundary grid is illustrated in Fig. 2.17. Its compact difference equation is

$$f'_0 + \alpha_b f'_1 = \frac{1}{h} (a_b f_{-1/2} + b_b f_{1/2} + c_b f_{3/2} + d_b f_{5/2} + e_b f_{7/2}) + \epsilon. \quad (2.63)$$

Relations among coefficients are

$$\begin{aligned} a_b &= \frac{\alpha_b - 22}{24}, b_b = \frac{-27\alpha_b + 17}{24}, c_b = \frac{9\alpha_b + 3}{8}, \\ d_b &= \frac{-\alpha_b - 5}{24}, e_b = \frac{1}{24}, \end{aligned} \quad (2.64)$$

and

$$\epsilon = \left(-\frac{3\alpha_b}{640} + \frac{71}{1920} \right) h^4 f^{(5)} + O(h^5). \quad (2.65)$$

By the similar consideration, we obtain the effective grid wave number w' for this type as

$$jw' = \frac{a_b e^{-jw/2} + b_b e^{jw/2} + c_b e^{j3w/2} + d_b e^{j5w/2} + e_b e^{j7w/2}}{1 + \alpha_b e^{jw}}. \quad (2.66)$$

The absolute value of amplitude error of the compact difference in the interval with 60 grid points is illustrated in Fig. 2.18. Here, the grid wave number is set to be $\pi/3$ (6 PPW). The parameter α_b in Eq.(2.64) for the inner grid points also is set to be the optimum value for the frequency range below 6 PPW. At the grid point on each boundary, α_b is set to be 8.21. Though the absolute value of the error is large at the grid point on each boundary, it is less than the other case. The maximum absolute value of relative amplitude error is also estimated on the boundary point in the frequency range below a specified upper bound. By a similar procedure to the previous case, the amplitude error is minimized to 2.68×10^{-2} when α_b takes a value around 8.212. However, the efficacy of the optimization is not large for 6 PPW.

From the discussions above, the dispersion error in the finite difference at the boundary grid point cannot be greatly improved when the grid spacing is not small enough compared to the wavelength to be considered.

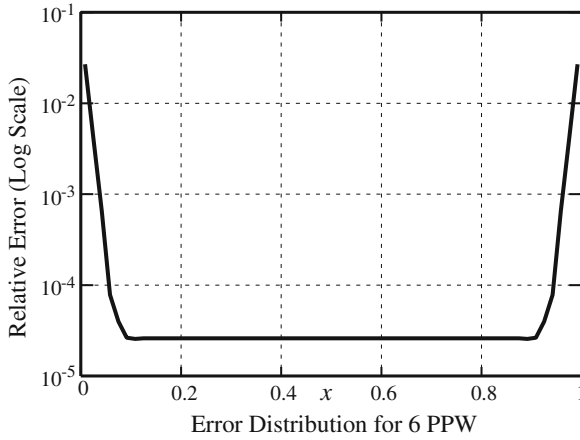


Fig. 2.18 Distribution of absolute value of relative amplitude error on the grid with 60 points. The grid wave number is set to be $\pi/3$ (6 PPW)

2.2.2 Improvement of Time Integration

Since the time integration must be fulfilled after evaluating spatial differentiations in FDTD, the next aim is to improve the time marching procedure. For the long time integrations, a symplectic integration method is an excellent scheme when the dynamics of the system possesses a Hamiltonian structure. The symplectic integration scheme is developed for the last few decades and is applied to particle dynamics and celestial mechanics. Higher order schemes of symplectic integration are considered by many authors. Extensions of the theory to a partial differential equation have been investigated recently. Here, we do not go far into theoretical details of the symplectic integration. Instead, the acoustic simulation is carried out by the symplectic integration keeping higher accuracy during long time steps.

We describe the outline of the symplectic integral method. When a set of ordinary differential equations for variables p and q are described by the following form:

$$\frac{dp}{dt} = f(q), \quad \frac{dq}{dt} = g(p), \quad (2.67)$$

the time marching by a time step Δt is carried out through m intermediate stages. The operations at i -th stage are

$$\begin{aligned} P_i &= P_{i-1} + \Delta t b_i f(Q_{i-1}), \\ Q_i &= Q_{i-1} + \Delta t \tilde{b}_i g(P_i), \end{aligned} \quad (2.68)$$

Table 2.2 Coefficients for Ruth's formula

	$i = 1$	$i = 2$	$i = 3$
b_i	7/24	3/4	-1/24
\tilde{b}_i	2/3	-2/3	1

where

$$\begin{aligned} P_0 &= p(t), Q_0 = q(t), \\ P_m &= p(t + \Delta t), Q_m = q(t + \Delta t). \end{aligned} \quad (2.69)$$

The coefficients b_i and \tilde{b}_i for Ruth's formula [13] are shown in Table 2.2.

For sound wave propagation, p and q are considered as acoustic pressure and velocity vector \mathbf{v} , respectively. Also, $f(q)$ and $g(p)$ are described by the compact finite differences in velocity vector \mathbf{v} and pressure p , respectively.

Simulations of one-dimensional wave propagation have been carried out. We have chosen the initial wave form $f(x)$ as

$$f(x) = \frac{1}{2} \exp[-\ln 2 (\frac{x}{3})^2] \quad (2.70)$$

on the grid whose spacing $h = 1.0$. The sound speed c is supposed as unity. We let the initial Gaussian form travel up to 10,000 time steps by using three different schemes. The shapes of the waves at several time steps simulated by various schemes are illustrated in Fig. 2.19. In each figure, the abscissa is $x' = x - ct$. The result obtained by the combination of optimized fourth-order compact finite difference ($\alpha = 0.1475$) and Ruth's time integration scheme is excellent. Even at the time step of 10,000, the wave shape almost retains the initial form by this scheme. Therefore, the symplectic method is an effective integration technique for long time step computations.

2.3 Application to Vibroacoustic Problems

In this section, application of the FDTD method to vibroacoustic problems such as a sound radiation problem and a structure-borne sound problem is presented. Herein two types of modeling methods for solid part like walls and floors, solid modeling and beam-plate modeling, are considered. The former is a straightforward method where longitudinal and shear waves are considered and solid part is discretized with many small volumes. Using the solid modeling, physical phenomena can be relatively well expressed but the computational cost will become huge. On the other hand, the latter considers solid part as a composition of plate elements. Therefore, longitudinal and bending waves are taken into account with plate theories. Although there are some limitations in applicability, this modeling has an advantage of the

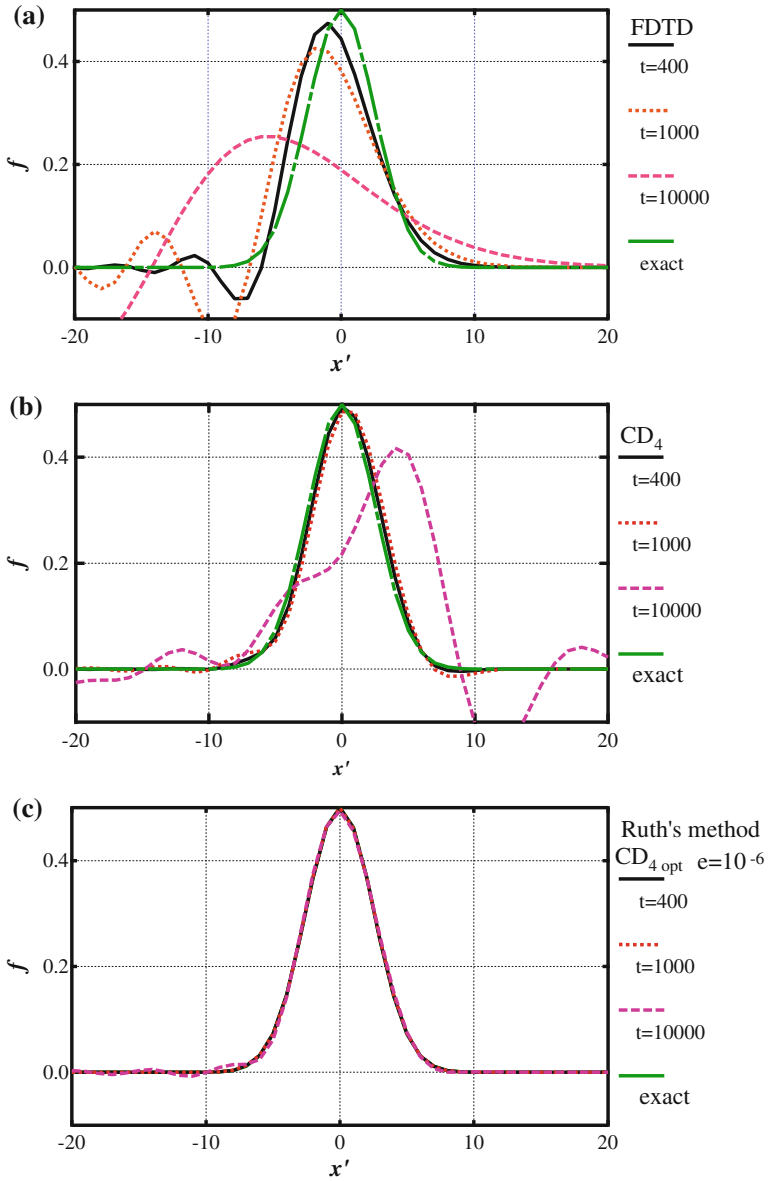


Fig. 2.19 Comparison of the wave forms at several time steps obtained by **a** the conventional FDTD scheme (explicit second-order finite difference and leap frog time integration) with CFL number 0.9, **b** the fourth-order compact finite difference and the leap frog time integration with CFL number = 0.25, and **c** the optimized fourth-order compact finite difference ($\alpha = 0.1475$) and Ruth's time integration with CFL number = 0.5

small computational load. The following introduce the formulations of vibroacoustic FDTD method according to the modeling method. Numerical examples of this section are shown in Sect. 7.6.

2.3.1 Solid Modeling

2.3.1.1 Basic Equations

To analyze vibrations of solid, consider equations of motion and constitutive equations of three-dimensional elastic bodies [14]. When probing vibration, one of the most important phenomena is damping. Many formulations and implementations have been suggested from various viewpoints, regardless if the medium is solid or fluid [15–18]. Herein two types of damping terms, which give distinct damping characteristics, are considered [19]. Then, under the conditions of small deformation, adiabatic transition, and athermic medium, the motion equations and constitutive equations with two types of damping terms can be expressed in tensor notation as [20]

$$\rho \frac{\partial v_i}{\partial t} + \zeta v_i = \frac{\partial T_{ij}}{\partial a_j}, \quad (2.71)$$

$$T_{ij} = c_{ijkl} \epsilon_{kl} + \xi_{ijkl} e_{kl}, \quad (2.72)$$

where $i, j, k, l = x, y, z$. ρ is the density, \mathbf{v} is the velocity vector, and t is time. ζ is a constant to describe the damping force proportional only to the velocity, while \mathbf{T} is the stress tensor. \mathbf{a} ($= [x, y, z]$) is the position vector, \mathbf{c} is the stiffness tensor, and $\boldsymbol{\epsilon}$ is the strain tensor. $\boldsymbol{\xi}$ is the viscosity tensor, which describes the damping force proportional to the second-order space derivative of the velocity, and \mathbf{e} ($= \partial \boldsymbol{\epsilon} / \partial t$) is the strain velocity tensor. It should be noted that combining the two types of damping terms ζ and $\boldsymbol{\xi}$ yields similar characteristics to Rayleigh damping [21]. Considering the reciprocities of stiffness and viscosity, stiffness tensor \mathbf{c} and viscosity tensor $\boldsymbol{\xi}$ can be abbreviated to their six-by-six matrix forms, each of which has 21 independent constants.

Additionally, if an orthotropic medium is considered, the constants can be reduced to nine independent ones. In this case, the relationship between the stiffness matrix \mathbf{C} and Young's modulus E , shear modulus G , and Poisson's ratios ν can be given by

$$\mathbf{C} = \mathbf{S}^{-1}, \quad (2.73)$$

$$\frac{\nu_{yz}}{E_y} = \frac{\nu_{zy}}{E_z}, \frac{\nu_{zx}}{E_z} = \frac{\nu_{xz}}{E_x}, \frac{\nu_{xy}}{E_x} = \frac{\nu_{yx}}{E_y}, \quad (2.74)$$

$$\mathbf{S} = \begin{bmatrix} \frac{1}{E_x} & -\frac{\nu_{xy}}{E_x} & -\frac{\nu_{xz}}{E_x} & 0 & 0 & 0 \\ -\frac{\nu_{yx}}{E_y} & \frac{1}{E_y} & -\frac{\nu_{yz}}{E_y} & 0 & 0 & 0 \\ -\frac{\nu_{zx}}{E_z} & -\frac{\nu_{zy}}{E_z} & \frac{1}{E_z} & 0 & 0 & 0 \\ 0 & 0 & 0 & \frac{1}{G_{yz}} & 0 & 0 \\ 0 & 0 & 0 & 0 & \frac{1}{G_{zx}} & 0 \\ 0 & 0 & 0 & 0 & 0 & \frac{1}{G_{xy}} \end{bmatrix}, \quad (2.75)$$

where \mathbf{S} is the compliance matrix. When dealing with vibroacoustic problems, behaviors of a fluid should be described with its basic equations. Interestingly, although Eqs. (2.71) and (2.72) with a stiffness matrix are derived for a solid, they can also express governing equations of a fluid with an appropriate stiffness matrix, i.e., the bulk modulus κ and zero should be substituted for $c_{11} = c_{22} = c_{33} = c_{12} = c_{21} = c_{13} = c_{31} = c_{23} = c_{32}$ and the other components of \mathbf{c} , respectively[22]. In this case, Eq. (2.72) can be interpreted as the constitutive equation of a Newtonian fluid. The linearized Navier–Stokes equation where the convection term and volumetric force are neglected can be derived by neglecting the term ζv_i of Eq. (2.71) and substituting Eq. (2.72) into Eq. (2.71). As for damping terms, $\chi \equiv \xi_{12} = \xi_{21} = \xi_{13} = \xi_{31} = \xi_{23} = \xi_{32}$ mean the second viscosity [23] and $\gamma \equiv \xi_{44} = \xi_{55} = \xi_{66}$ mean the shear viscosity, then $\xi_{11} = \xi_{22} = \xi_{33}$ can be written as $\chi + 2\gamma$. Note that the dilatational viscosity can be expressed as $\chi + (2/3)\gamma$. The sound pressure can be obtained by calculating $-\kappa \nabla \cdot \mathbf{u}$, where \mathbf{u} is the displacement vector that can be calculated by integrating the velocity vector \mathbf{v} over time.

For discretization with a difference scheme of the leap-frog algorithm, Eqs. (2.71) and the time-derivative form of (2.72) are rewritten as

$$\rho \frac{\partial v_x}{\partial t} + \zeta v_x = \frac{\partial T_{xx}}{\partial x} + \frac{\partial T_{xy}}{\partial y} + \frac{\partial T_{zx}}{\partial z}, \quad (2.76)$$

$$\rho \frac{\partial v_y}{\partial t} + \zeta v_y = \frac{\partial T_{xy}}{\partial x} + \frac{\partial T_{yy}}{\partial y} + \frac{\partial T_{yz}}{\partial z}, \quad (2.77)$$

$$\rho \frac{\partial v_z}{\partial t} + \zeta v_z = \frac{\partial T_{zx}}{\partial x} + \frac{\partial T_{yz}}{\partial y} + \frac{\partial T_{zz}}{\partial z}, \quad (2.78)$$

$$\begin{aligned} \frac{\partial T_{xx}}{\partial t} &= c_{11} \frac{\partial v_x}{\partial x} + c_{12} \frac{\partial v_y}{\partial y} + c_{13} \frac{\partial v_z}{\partial z} \\ &\quad + \xi_{11} \frac{\partial^2 v_x}{\partial x \partial t} + \xi_{12} \frac{\partial^2 v_y}{\partial y \partial t} + \xi_{13} \frac{\partial^2 v_z}{\partial z \partial t}, \end{aligned} \quad (2.79)$$

$$\frac{\partial T_{yy}}{\partial t} = c_{12} \frac{\partial v_x}{\partial x} + c_{22} \frac{\partial v_y}{\partial y} + c_{23} \frac{\partial v_z}{\partial z}$$

$$+ \xi_{12} \frac{\partial^2 v_x}{\partial x \partial t} + \xi_{22} \frac{\partial^2 v_y}{\partial y \partial t} + \xi_{23} \frac{\partial^2 v_z}{\partial z \partial t}, \quad (2.80)$$

$$\begin{aligned} \frac{\partial T_{zz}}{\partial t} = & c_{13} \frac{\partial v_x}{\partial x} + c_{23} \frac{\partial v_y}{\partial y} + c_{33} \frac{\partial v_z}{\partial z} \\ & + \xi_{13} \frac{\partial^2 v_x}{\partial x \partial t} + \xi_{23} \frac{\partial^2 v_y}{\partial y \partial t} + \xi_{33} \frac{\partial^2 v_z}{\partial z \partial t}, \end{aligned} \quad (2.81)$$

$$\frac{\partial T_{yz}}{\partial t} = c_{44} \frac{\partial v_z}{\partial y} + c_{44} \frac{\partial v_y}{\partial z} + \xi_{44} \frac{\partial^2 v_z}{\partial y \partial t} + \xi_{44} \frac{\partial^2 v_y}{\partial z \partial t}, \quad (2.82)$$

$$\frac{\partial T_{zx}}{\partial t} = c_{55} \frac{\partial v_x}{\partial z} + c_{55} \frac{\partial v_z}{\partial x} + \xi_{55} \frac{\partial^2 v_x}{\partial z \partial t} + \xi_{55} \frac{\partial^2 v_z}{\partial x \partial t}, \quad (2.83)$$

$$\frac{\partial T_{xy}}{\partial t} = c_{66} \frac{\partial v_y}{\partial x} + c_{66} \frac{\partial v_x}{\partial y} + \xi_{66} \frac{\partial^2 v_y}{\partial x \partial t} + \xi_{66} \frac{\partial^2 v_x}{\partial y \partial t}, \quad (2.84)$$

where v_x is the x -directional velocity, v_y is the y -directional velocity, and v_z is the z -directional velocity. T_{xx} is the x -directional normal stress, T_{yy} is the y -directional normal stress, and T_{zz} is the z -directional normal stress. T_{yz} is the shear stress defined in the yz -plane, T_{zx} is the shear stress defined in the zx -plane, and T_{xy} is the shear stress defined in the xy -plane.

2.3.1.2 Averaging of Material Parameters

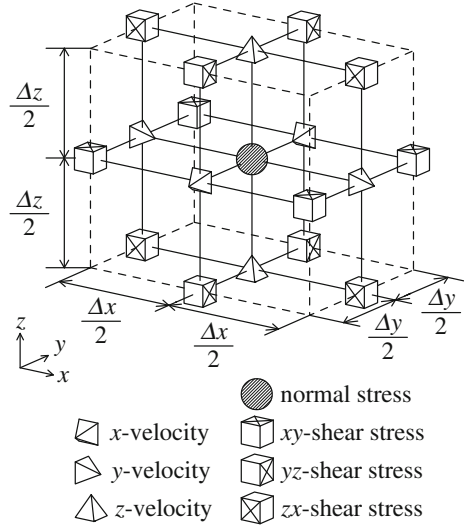
Figure 2.20 shows the arrangement of reference points for the stress and velocity on a nonuniform staggered-grid system [24–27]. Δx , Δy , and Δz are the spatial intervals between the reference points of shear stress and velocity for the x , y , and z directions. Point locations of normal stress are expressed as i , j , and k , while point locations of shear stress and velocity should shift according to the staggered-grid system. For example, the point locations of the xy -shear stress are expressed as $i + 0.5$, $j + 0.5$, and k , whereas those of the x -velocity are expressed as $i + 0.5$, j , and k . Δt is the time interval for the calculation, and the elapsed-time counter is given by superscript n for normal and shear stresses and $n + 0.5$ for velocities.

The target region of a vibroacoustic problem can be filled with a heterogeneous orthotropic material, which is governed by Eqs. (2.71) and (2.72). Herein, all the material parameters are defined at the reference points of normal stress, and the mean values are used as reference points for shear stress and velocity [28–32]. The weighted arithmetic averages are employed at the reference points of velocity [33], for example,

$$\bar{\rho}(i + 0.5, j, k) = \frac{\rho(i, j, k) \Delta x(i) + \rho(i + 1, j, k) \Delta x(i + 1)}{\Delta x(i) + \Delta x(i + 1)}. \quad (2.85)$$

At the reference points of shear stress, the weighted harmonic averages are employed [33], for example,

Fig. 2.20 Yee cell which has spatial intervals of Δx , Δy , and Δz



$$\begin{aligned} \overline{G_{xy}}(i + 0.5, j + 0.5, k) \\ = \frac{\{\Delta x(i) + \Delta x(i + 1)\}\{\Delta y(j) + \Delta y(j + 1)\}}{\frac{\Delta x(i)\Delta y(j)}{G_{xy}(i, j, k)} + \frac{\Delta x(i+1)\Delta y(j)}{G_{xy}(i+1, j, k)} + \frac{\Delta x(i)\Delta y(j+1)}{G_{xy}(i, j+1, k)} + \frac{\Delta x(i+1)\Delta y(j+1)}{G_{xy}(i+1, j+1, k)}}. \end{aligned} \quad (2.86)$$

Additionally, the damping constants are given by their arithmetic averages at the velocity points and by their harmonic averages at the shear-stress points.

2.3.1.3 Boundary Conditions

A general method should accommodate a variety of boundary conditions such as a fixed boundary, free boundary, and perfectly absorptive boundary. For absorptive boundary, PML would be the most reliable option [34]. Implementation of the PML to this method is introduced in reference [19, 20]. Hence, this section focuses on two boundaries: a fixed boundary and a free boundary [33].

A fixed boundary is considered to be the boundary with the rigid body, which has infinite density and infinite shear modulus. Therefore, the averaged density as shown in Eq. (2.85) becomes infinite and then the velocity normal to the fixed surface becomes zero. This condition can be directly satisfied for the reference points of velocity located on the boundary. However, because the reference points of the velocity components parallel to the boundary surface are not defined just on the boundary, virtual reference points are assumed outside the boundary, and their values are determined so that the mean velocities on the boundary are zero. For example, if the plane $i + 0.5 = I + 0.5$ is assumed to be a fixed boundary, then

$$v_x(I + 0.5, j, k) = 0, \quad (2.87)$$

$$v_y(I, j \pm 0.5, k) + v_y(I + 1, j \pm 0.5, k) = 0, \quad (2.88)$$

$$v_z(I, j, k \pm 0.5) + v_z(I + 1, j, k \pm 0.5) = 0. \quad (2.89)$$

Additionally, in Eq. (2.86), the related term to the rigid body in the denominator becomes zero. For example, the averaged shear modulus on the fixed boundary with a uniform mesh becomes $4G/3$ when one of the adjacent four media is the rigid body and the others have the same shear modulus G .

On the other hand, a free boundary is considered to be the boundary with vacuum, where the density and shear modulus are zero. The averaged shear modulus as shown in Eq. (2.86) becomes zero and then the shear stress defined in the free surface becomes zero. Although the normal stress to the boundary surface must be zero as a matter of course, the reference points of normal stress, which should be zero, are not arranged on the boundary. Therefore, virtual reference points are assumed outside the boundary, and their values are determined such that the mean normal stresses on the boundary are zero. For example, if the plane $i + 0.5 = I + 0.5$ is assumed to be a free boundary, then

$$T_{xy}(I + 0.5, j \pm 0.5, k) = T_{zx}(I + 0.5, j, k \pm 0.5) = 0, \quad (2.90)$$

$$T_{xx}(I, j, k) + T_{xx}(I + 1, j, k) = 0. \quad (2.91)$$

Additionally, the related term to vacuum in the numerator in Eq. (2.85) becomes zero. For example, the averaged density on the free boundary with an uniform mesh becomes $\rho/2$ when one of the adjacent two media is vacuum and the other has a density ρ .

2.3.1.4 Discretization

For example, Eq. (2.76) is discretized with a central difference as

$$\begin{aligned} & \bar{\rho}(i + 0.5, j, k) \frac{v_x^{n+0.5}(i + 0.5, j, k) - v_x^{n-0.5}(i + 0.5, j, k)}{\Delta t} \\ & + \bar{\zeta}(i + 0.5, j, k) \frac{v_x^{n+0.5}(i + 0.5, j, k) + v_x^{n-0.5}(i + 0.5, j, k)}{2} \\ & \approx \frac{T_{xx}^n(i + 1, j, k) - T_{xx}^n(i, j, k)}{\{\Delta x(i + 1) + \Delta x(i)\}/2} \\ & + \frac{T_{xy}^n(i, j + 0.5, k) - T_{xy}^n(i, j - 0.5, k)}{\Delta y(j)} \\ & + \frac{T_{zx}^n(i, j, k + 0.5) - T_{zx}^n(i, j, k - 0.5)}{\Delta z(k)}. \end{aligned} \quad (2.92)$$

Eq. (2.84) is discretized with a backward difference for time derivation of the viscosity term and central difference for other terms as

$$\begin{aligned}
 & \frac{T_{xy}^{n+1}(i+0.5, j+0.5, k) - T_{xy}^n(i+0.5, j+0.5, k)}{\Delta t} \\
 & \approx \left\{ \overline{c_{66}}(i+0.5, j+0.5, k) + \frac{\overline{\xi_{66}}(i+0.5, j+0.5, k)}{\Delta t} \right\} \\
 & \times \frac{v_y^{n+0.5}(i+1, j+0.5, k) - v_y^{n+0.5}(i, j+0.5, k)}{\{\Delta x(i+1) + \Delta x(i)\}/2} \\
 & - \frac{\overline{\xi_{66}}(i+0.5, j+0.5, k)}{\Delta t} \\
 & \times \frac{v_y^{n-0.5}(i+1, j+0.5, k) - v_y^{n-0.5}(i, j+0.5, k)}{\{\Delta x(i+1) + \Delta x(i)\}/2} \\
 & + \left\{ \overline{c_{66}}(i+0.5, j+0.5, k) + \frac{\overline{\xi_{66}}(i+0.5, j+0.5, k)}{\Delta t} \right\} \\
 & \times \frac{v_x^{n+0.5}(i+0.5, j+1, k) - v_x^{n+0.5}(i+0.5, j, k)}{\{\Delta y(j+1) + \Delta y(j)\}/2} \\
 & - \frac{\overline{\xi_{66}}(i+0.5, j+0.5, k)}{\Delta t} \\
 & \times \frac{v_x^{n-0.5}(i+0.5, j+1, k) - v_x^{n-0.5}(i+0.5, j, k)}{\{\Delta y(j+1) + \Delta y(j)\}/2}. \tag{2.93}
 \end{aligned}$$

Transforming these discretized equations, updating formulas for $v_x^{n+0.5}(i+0.5, j, k)$ and $T_{xy}^{n+1}(i+0.5, j+0.5, k)$ can be obtained. Updating formulas for other variables can be obtained by a similar procedure.

2.3.1.5 Stability Condition

This section focuses on stability conditions considering orthotropic media. An arbitrary wave can be expressed as a superposition of plane waves. Hence, the stability conditions for a plane wave of an arbitrary propagation angle are derived here [35]. The velocities and stress for a plane wave can be expressed as

$$v_x^{n+0.5}(i+0.5, j, k) = v_{x0}^{n+0.5} e^{i\{k_x(i+0.5)\Delta x + k_y j \Delta y + k_z k \Delta z\}}, \tag{2.94}$$

$$T_{xx}^n(i, j, k) = T_{xx0}^n e^{i(k_x i \Delta x + k_y j \Delta y + k_z k \Delta z)}, \tag{2.95}$$

$$T_{xy}^n(i+0.5, j+0.5, k) = T_{xy0}^n e^{i\{k_x(i+0.5)\Delta x + k_y(j+0.5)\Delta y + k_z k \Delta z\}}, \tag{2.96}$$

where i is an imaginary unit, and k_x , k_y , and k_z are x , y , and z -directional wave numbers, respectively. Substituting Eqs. (2.94)–(2.96) into Eqs. (2.76)–(2.84) yields a homogeneous state-difference equation, which is expressed as

$$\mathbf{x}^{n+1} = \mathbf{A}\mathbf{x}^n, \quad (2.97)$$

where

$$[\mathbf{x}^n]^* = \begin{bmatrix} v_{x0}^{n-0.5} & v_{y0}^{n-0.5} & v_{z0}^{n-0.5} & T_{xx0}^n & T_{yy0}^n & T_{zz0}^n & T_{yz0}^n & T_{zx0}^n & T_{xy0}^n \end{bmatrix}, \quad (2.98)$$

$$\mathbf{A} = \begin{bmatrix} r_x & 0 & 0 & R_x h_x & 0 & 0 & & & \\ 0 & r_y & 0 & 0 & R_y h_y & 0 & & & \\ 0 & 0 & r_z & 0 & 0 & R_z h_z & & & \\ b_{11x} h_x & b_{12y} h_y & b_{13z} h_z & 1 - B_{11x} h_x^2 & -B_{12y} h_y^2 & -B_{13z} h_z^2 & & & \\ b_{12x} h_x & b_{22y} h_y & b_{23z} h_z & -B_{12x} h_x^2 & 1 - B_{22y} h_y^2 & -B_{23z} h_z^2 & & & \\ b_{13x} h_x & b_{23y} h_y & b_{33z} h_z & -B_{13x} h_x^2 & -B_{23y} h_y^2 & 1 - B_{33z} h_z^2 & & & \\ 0 & b_{44x} h_x & b_{44y} h_y & 0 & -B_{44x} h_x h_y & -B_{44y} h_y h_z & & & \\ b_{55x} h_z & 0 & b_{55x} h_x & -B_{55x} h_z h_x & 0 & -B_{55x} h_z h_x & & & \\ b_{66x} h_y & b_{66x} h_x & 0 & -B_{66x} h_x h_y & -B_{66x} h_x h_y & 0 & & & \\ 0 & & R_x h_z & & R_x h_y & & & & \\ R_y h_z & & 0 & & R_y h_x & & & & \\ R_z h_y & & R_z h_x & & 0 & & & & \\ -(B_{12y} + B_{13z}) h_y h_z & & -(B_{13z} + B_{11x}) h_z h_x & & -(B_{11x} + B_{12y}) h_x h_y & & & & \\ -(B_{22y} + B_{23z}) h_y h_z & & -(B_{23z} + B_{12x}) h_z h_x & & -(B_{12x} + B_{22y}) h_x h_y & & & & \\ -(B_{23y} + B_{33z}) h_y h_z & & -(B_{33z} + B_{13x}) h_z h_x & & -(B_{13x} + B_{23y}) h_x h_y & & & & \\ 1 - B_{44z} h_y^2 - B_{44y} h_z^2 & & -B_{44z} h_x h_y & & -B_{44y} h_z h_x & & & & \\ -B_{55z} h_x h_y & & 1 - B_{55x} h_z^2 - B_{55z} h_x^2 & & -B_{55x} h_y h_z & & & & \\ -B_{66y} h_z h_x & & -B_{66x} h_y h_z & & 1 - B_{66y} h_x^2 - B_{66x} h_y^2 & & & & \end{bmatrix}, \quad (2.99)$$

$$\theta = \frac{\Delta t}{2\rho} \zeta, \quad (2.100)$$

$$r = \frac{1 - \theta}{1 + \theta}, \quad (2.101)$$

$$R = \frac{i\Delta t}{\rho(1 + \theta)}, \quad (2.102)$$

$$b_\alpha = i\Delta t \left\{ \frac{c_\alpha(1 - \theta) - 2\xi_\alpha\theta}{1 + \theta} \right\}, \quad (2.103)$$

$$B_\alpha = \frac{c_\alpha \Delta t^2 - \xi_\alpha \Delta t}{\rho(1 + \theta)}, \quad (2.104)$$

$$h_d = \frac{2 \sin \left(k_d \frac{\Delta d_{\min}}{2} \right)}{\Delta d_{\min}}, \quad (2.105)$$

where the asterisk denotes the transpose, $\alpha = 11, 22, 33, 12, 13, 23, 44, 55$, and 66 , $d = x, y, z$, and subscript min means the minimum value. To obtain stable solutions from Eq. (2.97), all eigenvalues must be equal to or less than one for an arbitrary propagation angle, i.e., for the arbitrary coupling of k_x , k_y , and k_z . Therefore, assigning h_x , h_y , and h_z to their maximum values of $2/\Delta x_{\min}$, $2/\Delta y_{\min}$, and $2/\Delta z_{\min}$, respectively, should yield Δt such that all eigenvalues of matrix A are one or less.

2.3.1.6 Initial Condition and Excitation

Herein all initial values of velocities and stresses are set to zero and an input excitation is assumed to be a point force $F(t)$ at the cell indicated by i , j , and k . In this case, $F(n\Delta t)/\Delta S(i, j, k)$ should be added to the normal stress in the excitation direction, which belongs to the spatial difference term in the updating formula of velocity. $\Delta S(i, j, k)$ is the unit area normal to the excitation direction, for example, $\Delta S(i, j, k) = \Delta y(j) \Delta z(k)$ for x -directional excitation.

2.3.2 Plate Modeling

2.3.2.1 Basic Equations

Governing equations for the bending wave and the quasi-longitudinal wave on a plate model are described as follows. Equation (2.106) describes the bending wave propagation on the plate existing in the $x - y$ plane, and Eqs. (2.107) and (2.108) describe the in-plane wave for the x and y direction.

$$D \left(\frac{\partial^2}{\partial x^2} + \frac{\partial^2}{\partial y^2} \right)^2 w + \xi D \frac{\partial}{\partial t} \left(\frac{\partial^2}{\partial x^2} + \frac{\partial^2}{\partial y^2} \right)^2 w + \rho h \mu \frac{\partial w}{\partial t} + \rho h \frac{\partial^2 w}{\partial t^2} = q, \quad (2.106)$$

$$\frac{E}{1 - \gamma^2} \left(\frac{\partial^2 u}{\partial x^2} + \gamma \frac{\partial^2 v}{\partial x \partial y} \right) + G \left(\frac{\partial^2 v}{\partial x \partial y} + \frac{\partial^2 u}{\partial y^2} \right) - \rho \frac{\partial^2 u}{\partial t^2} = 0, \quad (2.107)$$

$$\frac{E}{1 - \gamma^2} \left(\frac{\partial^2 v}{\partial y^2} + \gamma \frac{\partial^2 u}{\partial x \partial y} \right) + G \left(\frac{\partial^2 u}{\partial x \partial y} + \frac{\partial^2 v}{\partial x^2} \right) - \rho \frac{\partial^2 v}{\partial t^2} = 0. \quad (2.108)$$

Here, w is the displacement of the out-of-plane bending vibration, u and v are those of the in-plane vibration in the x and y directions, ξ and μ are coefficients for modeling the damping characteristics of the material, q is an external force, D is the flexural

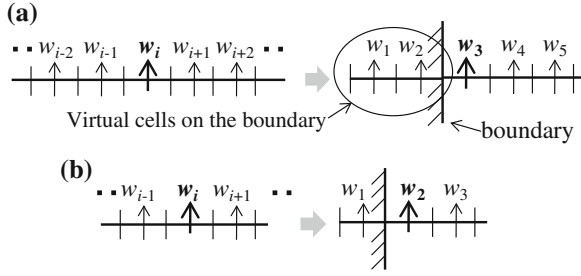


Fig. 2.21 Schematic figure for the finite-difference approximation nearby the boundary part in case of fourth-/second-order differentials. **a** 4th-order differential, **b** 2nd-order differential

rigidity ($D = Eh^3/12(1 - \gamma^2)$), and E , ρ , h , γ and G are the Young's modulus, density, thickness of the plate, the Poisson's ratio, and the elastic shear modulus, respectively.

2.3.2.2 Discretization

The basic equations of Eq. (2.106)/Eq. (2.107) and (2.108) for the bending/in-plane wave has fourth-order/second-order differential system. Finite-difference approximation of the fourth-order/second-order differential for a function $w(x)$ is described as

$$\frac{\partial^4 w_i}{\partial x^4} = \frac{w_{i+2} - 4w_{i+1} + 6w_i - 4w_{i-1} + w_{i-2}}{\Delta x^4} + O(\Delta x^2), \quad (2.109)$$

$$\frac{\partial^2 w_i}{\partial x^2} = \frac{w_{i+1} - 2w_i + w_{i-1}}{\Delta x^2} + O(\Delta x^2), \quad (2.110)$$

where i is the discrete grid number in space. Equation (2.109) indicates that a parameter w_i is calculated using the neighboring five parameters including itself, as show in Fig. 2.21. As for Eq. (2.110) w_i is calculated using the neighboring three parameters. When we calculate the parameter w_3 in Fig. 2.21a or w_2 in Fig. 2.21b defined at the boundary part, two or one virtual cells must be considered for each situation. A boundary condition of the plate can be modeled by setting appropriate values for the virtual parameters. For example, the fixed edge condition for bending motion of a plate can be simulated by setting 0 for both virtual parameters on the boundary.

In case a vibration model is composed of two plate elements which are rigidly connected with each other, the vibration transmission through each element can be simulated by considering the relationship between the virtual parameters defined at the boundary belonging to each plate. Then, the relationship of the parameters is defined based on the continuity conditions concerning the bending and the in-plane wave motion of each plate. Detailed procedure is described in the next section. Spatial

and time differential terms in the governing equations described above are approximated by finite difference, and time development of the bending/in-plane wave is calculated by an implicit method. The procedure of the approximation for the basic equations are shown herein. The space derivative of the parameter is approximated by central difference method, and time derivative of that is approximated by following one-sided differencing approximation:

$$\frac{\partial^2 w^{n+1}}{\partial x^2} = \frac{2w^{n+1} - 5w^n + 4w^{n-1} - w^{n-2}}{\Delta t^2} + O(\Delta t^2), \quad (2.111)$$

where n indicates the time step. As a result of the approximation, a discretized equation is obtained. Transforming the equations, updating formula for the out-of-plane displacement is described as follows. In this equation, the parameters at the time step of $n + 1$ in the left side are unknown, and those at the time steps of n , $n - 1$ and $n - 2$ on the right side are already known parameters.

$$(2 + \mu \Delta t) + \left(1 + \frac{\xi}{\Delta t}\right) \Delta t^2 \frac{D}{\rho h} A^{n+1} = \frac{q_{i,j}^n}{\rho h} \Delta t^2 + (5 + \mu \Delta t) w_{i,j}^n - 4w_{i,j}^{n-1} + w_{i,j}^{n-2} + \frac{\xi D}{\rho h} \Delta t A^n, \quad (2.112)$$

where

$$\begin{aligned} A^n = & \left(\frac{w_{i+2,j}^n - 4w_{i+1,j}^n + 6w_{i,j}^n - 4w_{i-1,j}^n + w_{i-2,j}^n}{\Delta x^4} \right. \\ & + \frac{w_{i,j+2}^n - 4w_{i,j+1}^n + 6w_{i,j}^n - 4w_{i,j-1}^n + w_{i,j-2}^n}{\Delta y^4} \\ & + 2 \frac{(w_{i+1,j+1}^n - 2w_{i+1,j}^n + w_{i+1,j-1}^n) - 2(w_{i,j+1}^n - 2w_{i,j}^n + w_{i,j-1}^n)}{\Delta x^2 \Delta y^2} \\ & \left. + \frac{(w_{i-1,j+1}^n - 2w_{i-1,j}^n + w_{i-1,j-1}^n)}{\Delta x^2 \Delta y^2} \right). \end{aligned} \quad (2.113)$$

Following the same procedure, the discretized equations of the quasi-longitudinal wave for the x and y directions derived from Eqs. (2.107) and (2.108) are described as

$$\begin{aligned}
& -2u_{i,j}^{n+1} + \frac{E\Delta t^2}{(1-\gamma^2)\rho} \left(\frac{u_{i+1,j}^{n+1} - 2u_{i,j}^{n+1} + u_{i-1,j}^{n+1}}{\Delta x^2} \right. \\
& \quad \left. + \gamma \frac{(v_{i+1,j+1}^{n+1} - v_{i+1,j-1}^{n+1}) - (v_{i-1,j+1}^{n+1} - v_{i-1,j-1}^{n+1})}{2\Delta x \cdot 2\Delta y} \right) \\
& \quad + \frac{G\Delta t^2}{\rho} \left(\frac{u_{i,j+1}^{n+1} - 2u_{i,j}^{n+1} + u_{i,j-1}^{n+1}}{\Delta y^2} \right. \\
& \quad \left. + \frac{(v_{i+1,j+1}^{n+1} - v_{i+1,j-1}^{n+1}) - (v_{i-1,j+1}^{n+1} - v_{i-1,j-1}^{n+1})}{2\Delta x \cdot 2\Delta y} \right) \\
& = -5u_{i,j}^n + 4u_{i,j}^{n-1} - u_{i,j}^{n-2}, \tag{2.114}
\end{aligned}$$

$$\begin{aligned}
& -2v_{i,j}^{n+1} + \frac{E\Delta t^2}{(1-\gamma^2)\rho} \left(\frac{v_{i,j+1}^{n+1} - 2v_{i,j}^{n+1} + v_{i,j-1}^{n+1}}{\Delta x^2} \right. \\
& \quad \left. + \gamma \frac{(u_{i+1,j+1}^{n+1} - u_{i+1,j-1}^{n+1}) - (u_{i-1,j+1}^{n+1} - u_{i-1,j-1}^{n+1})}{2\Delta x \cdot 2\Delta y} \right) \\
& \quad + \frac{G\Delta t^2}{\rho} \left(\frac{v_{i+1,j}^{n+1} - 2v_{i,j}^{n+1} + v_{i-1,j}^{n+1}}{\Delta x^2} \right. \\
& \quad \left. + \frac{(u_{i+1,j+1}^{n+1} - u_{i+1,j-1}^{n+1}) - (v_{i-1,j+1}^{n+1} - v_{i-1,j-1}^{n+1})}{2\Delta x \cdot 2\Delta y} \right) \\
& = -5v_{i,j}^n + 4v_{i,j}^{n-1} - v_{i,j}^{n-2}, \tag{2.115}
\end{aligned}$$

where i and j indicate the discrete grid number in the x and y direction. To protect symmetry, discretization for the first-order differentiation in Eqs. (2.114) and (2.115) are performed based on the following equation:

$$\frac{\partial w_i}{\partial x} = \frac{w_{i+1} - w_{i-1}}{2\Delta x} + O(4\Delta x^2). \tag{2.116}$$

Finally, the obtained discrete equations and the continuity conditions for the junctions between elements are solved as simultaneous equations. Details of the procedure are described in the following section.

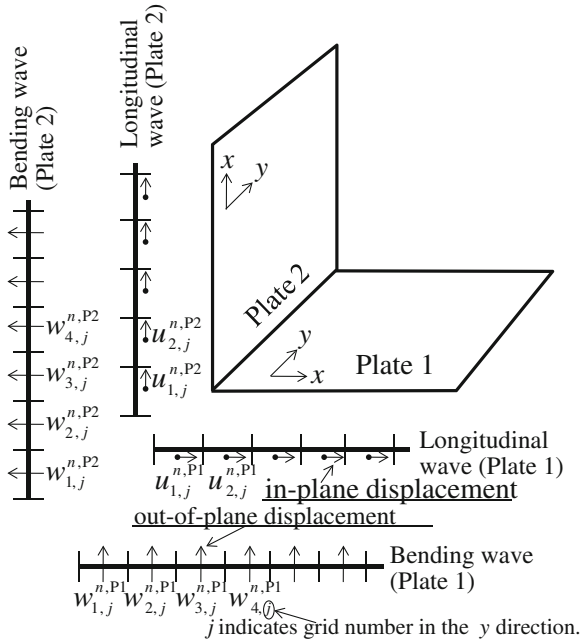


Fig. 2.22 Schematic figure and one-dimensional discrete form of a plate model

2.3.2.3 Composite Model with Multiple Plate Elements

In order to simulate a vibration model in which multiple plates are rigidly connected to each other, continuity conditions for vibration propagation at the joint part should be considered. In this section, the connecting method is described.

In Fig. 2.22, an axonometric view of the target plate model and a schematic figure, in which the three-dimensional model is illustrated in a one-dimensional discrete form, are shown. In the figure of the one-dimensional discrete form, $w_{1,j}^{n,P1}$, $w_{2,j}^{n,P1}$, $w_{3,j}^{n,P1}$ and $w_{4,j}^{n,P1}$ indicate the out-of-plane displacements in the time step of n , caused by bending deformation of Plate 1, and they are defined nearby the junction part. $w_{1,j}^{n,P2}$, $w_{2,j}^{n,P2}$, $w_{3,j}^{n,P2}$ and $w_{4,j}^{n,P2}$ indicate the out-of-plane displacements of Plate 2. $u_{1,j}^{n,P1}$, $u_{2,j}^{n,P1}$ and $u_{1,j}^{n,P2}$ and $u_{2,j}^{n,P2}$ indicate the in-plane displacements caused by in-plane deformation of Plate 1 and Plate 2, respectively. The parameter j attached in the subscript of each parameter indicates the grid number in the y -direction. In the simulation, continuity conditions described below are considered. First, the physical parameters of the displacement and the rotation angle at the boundary of Plate 1 are made to be equal to those of Plate 2. Second, the bending moments acting at the boundary of both Plate 1 and 2 are balanced. Lastly, the shear force acting at the boundary of Plate 1 and the in-plane force acting at the boundary of Plate 2 are also balanced. Totally, four conditions are considered. Here, the rotational angle

θ_b , bending moment M_x , shear force F_x , and in-plane force T_x are described by the following equations.

$$\theta_b = \frac{\partial w}{\partial x}, \quad (2.117)$$

$$M_x = -D \left(\frac{\partial^2 w}{\partial x^2} + \gamma \frac{\partial^2 w}{\partial y^2} \right), \quad (2.118)$$

$$F_x = -D \left(\frac{\partial^3 w}{\partial x^3} + (2 - \gamma) \frac{\partial^3 w}{\partial x \partial y^2} \right), \quad (2.119)$$

$$T_x = \frac{Eh}{1 - \gamma^2} \left(\frac{\partial u}{\partial x} + \gamma \frac{\partial v}{\partial y} \right). \quad (2.120)$$

These equations are transformed to discrete forms, and are rewritten by considering the continuity conditions.

1. Displacement:

$$\frac{3}{2}w_{2,j}^{n,P1} - \frac{1}{2}w_{1,j}^{n,P1} = \frac{u_{1,j}^{n,P2} + u_{2,j}^{n,P2}}{2}, \quad (2.121)$$

$$\frac{3}{2}w_{2,j}^{n,P2} - \frac{1}{2}w_{1,j}^{n,P2} = -\frac{u_{1,j}^{n,P1} + u_{2,j}^{n,P1}}{2}. \quad (2.122)$$

2. Rotational angle:

$$\frac{w_{2,j}^{n,P2} - w_{1,j}^{n,P2}}{\Delta x_{P2}} = \frac{w_{2,j}^{n,P1} - w_{1,j}^{n,P1}}{\Delta x_{P1}}. \quad (2.123)$$

3. Bending moment:

$$\begin{aligned} & \frac{w_{3,j}^{n,P2} - 2w_{2,j}^{n,P2} + w_{1,j}^{n,P2}}{\Delta x_{P2}^2} + \gamma \frac{w_{2,j+1}^{n,P2} - 2w_{2,j}^{n,P2} + w_{2,j-1}^{n,P2}}{\Delta y_{P2}^2} \\ & + \frac{w_{3,j}^{n,P1} - 2w_{2,j}^{n,P1} + w_{1,j}^{n,P1}}{\Delta x_{P1}^2} + \gamma \frac{w_{2,j+1}^{n,P1} - 2w_{2,j}^{n,P1} + w_{2,j-1}^{n,P1}}{\Delta y_{P1}^2} = 0. \end{aligned} \quad (2.124)$$

4. Shear force and in-plane force:

$$\begin{aligned}
& -D \left(\frac{w_{4,j}^{n,P2} - 3w_{3,j}^{n,P2} + 3w_{2,j}^{n,P2} - w_{1,j}^{n,P2}}{\Delta x_{P2}^3} \right. \\
& \quad \left. + (2 - \gamma) \frac{(w_{3,j+1}^{n,P2} - 2w_{3,j}^{n,P2} + w_{3,j-1}^{n,P2}) - (w_{2,j+1}^{n,P2} - 2w_{2,j}^{n,P2} + w_{2,j-1}^{n,P2})}{\Delta x_{P2} \Delta y_{P2}^2} \right) \\
& \quad - \frac{Eh}{1 - \gamma^2} \left(\frac{u_{2,j}^{n,P1} - u_{1,j}^{n,P1}}{\Delta x_{P1}} + \gamma \frac{u_{2,j+1}^{n,P1} - u_{2,j}^{n,P1}}{\Delta y_{P1}} \right) = 0, \tag{2.125}
\end{aligned}$$

$$\begin{aligned}
& -D \left(\frac{w_{4,j}^{n,P1} - 3w_{3,j}^{n,P1} + 3w_{2,j}^{n,P1} - w_{1,j}^{n,P1}}{\Delta x_{P1}^3} \right. \\
& \quad \left. + (2 - \gamma) \frac{(w_{3,j+1}^{n,P1} - 2w_{3,j}^{n,P1} + w_{3,j-1}^{n,P1}) - (w_{2,j+1}^{n,P1} - 2w_{2,j}^{n,P1} + w_{2,j-1}^{n,P1})}{\Delta x_{P1} \Delta y_{P1}^2} \right) \\
& \quad + \frac{Eh}{1 - \gamma^2} \left(\frac{u_{2,j}^{n,P2} - u_{1,j}^{n,P2}}{\Delta x_{P2}} + \gamma \frac{u_{2,j+1}^{n,P2} - u_{2,j}^{n,P2}}{\Delta y_{P2}} \right) = 0. \tag{2.126}
\end{aligned}$$

Here, Pm shown in each superscript indicates Plate m , the spatial intervals Δx_{P1} and Δy_{P1} indicate the spatial intervals of Plate 1, and Δx_{P2} and Δy_{P2} indicate those of Plate 2. In these equations, each parameter indicates the in-plane or out-of-plane displacement shown in Fig. 2.22. Solutions of the six unknown parameters ($w_{1,j}^{n,P1}, w_{2,j}^{n,P1}, w_{1,j}^{n,P2}, w_{2,j}^{n,P2}, u_{1,j}^{n,P1}$ and $u_{1,j}^{n,P2}$) at the junction are solved by considering the six equations above. Then, these continuity equations and the discrete forms of Eqs. (2.112), (2.114), and (2.115) are solved together as simultaneous equations. These equations are solved in every time step, and time development of vibration is simulated. To solve the simultaneous equations, PARDISO [36], built in the Intel Math Kernel library, was used.

2.3.2.4 Vibroacoustic Coupling Method

To couple the vibration field on the plate and the sound field as shown in Fig. 2.23a, the following continuity conditions should be considered. First, the external pressure to the plate described in Eq. (2.112) is given as the difference of the sound pressure on both sides of the plate; $p_{i,j,k}^n$ and $p_{i-1,j,k}^n$, as shown in the Step 1 of Fig. 2.23b.

$$q_{j,k}^n = p_{i,j,k}^n - p_{i-1,j,k}^n. \tag{2.127}$$

In the next step, the bending motion of the plate is calculated based on the external pressure, and the displacement of the plate is obtained. Then, the velocity is calculated using the displacement and is given to the particle velocity in the sound field.

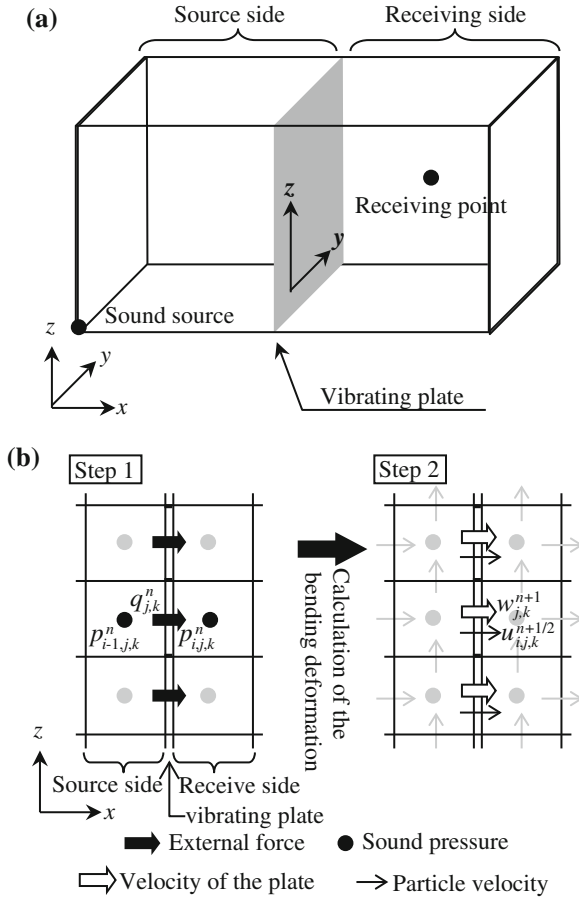


Fig. 2.23 Coupling method between the vibration and the sound

$$u_{i,j,k}^{n+1/2} = \frac{w_{j,k}^{n+1} - w_{j,k}^n}{\Delta t}, \quad (2.128)$$

where $w_{j,k}^n$ is the displacement of the plate. In case the normal impedance Z_n on the receiving side of the plate is considered, following relationship is used instead of Eq. (2.128).

$$u_{i,j,k}^{n+1/2} = \frac{w_{j,k}^{n+1} - w_{j,k}^n}{\Delta t} - \frac{p_{i,j,k}^n}{Z_n}. \quad (2.129)$$

To update the sound pressure and particle velocity in the sound field, high-order scheme using eight reference points is applied. Detailed method is described in the Ref. [37].

References

1. K.S. Yee, Numerical solution of initial boundary value problems involving Maxwell's equations in isotropic media. *IEEE Trans. Antennas Propag.* **17**, 585–589 (1966)
2. T. Yokota, S. Sakamoto, H. Tachibana, Visualization of sound propagation and scattering in rooms. *Acoust. Sci. Tech.* **23**(1), 40–46 (2002)
3. S. Sakamoto, H. Nagatomo, A. Ushiyama, H. Tachibana, Calculation of impulse responses and acoustic parameters in a hall by the finite-difference time-domain method. *Acoust. Sci. Tech.* **29**(4), 256–265 (2008)
4. D.M. Sullivan, A frequency-dependent FDTD method using Z transforms. *IEEE Trans. Antennas Propag.* **40**, 1223–1230 (1992)
5. J. Escolano, F. Jacobsen, J. Lopez, An efficient realization of frequency dependent boundary conditions in an acoustic finite-difference time-domain model. *J. Sound Vib.* **316**, 234–247 (2008)
6. H. Suzuki, A. Omoto, K. Fujiwara, Treatment of boundary conditions by finite difference time domain method. *Acoust. Sci. Tech.* **28**(1), 16–26 (2007)
7. T. Devezé, L. Beaulieu, W. Tabbara, A forth order scheme for the FDTD algorithm applied to Maxwell's equations. *IEEE Trans. Antennas Propag.* **42**, 859–862 (1994)
8. M.F. Hadi, M. Piket-May, S.L. Manry Jr., A modified FDTD (2,4) scheme for modeling electrically large structures with high phase accuracy. *IEEE Trans. Antennas Propag.* **45**, 254–264 (1997)
9. J. Von Neumann, R. Richtmyer, A method for the numerical calculation of hydrodynamic shock. *J. Appl. Phys.* **21**, 232–237 (1950)
10. G. Mur, Absorbing boundary conditions for the finite difference approximation of the time domain electromagnetic-field equation. *IEEE Trans. Electromagnetic Compat.* **EMC-23**(4), 377–382 (1981)
11. J.-P. Berenger, A perfectly matched layer for the absorption of electromagnetic waves. *J. Comput. Phys.* **114**, 185–200 (1994)
12. S.K. Lele, Compact finite difference scheme with spectral-like resolution. *J. Comput. Phys.* **103**, 16–42 (1992)
13. R.D. Ruth, A canonical integration technique. *IEEE. Trans. Mag.* **37**, 3251–3254 (2001)
14. B.A. Auld, *Acoustic Fields and Waves in Solids*, vol. 1, 2nd edn. (Krieger, Malabar, 1990)
15. L. Cremer, M. Heckl, B.A.T. Petersson, *Structure-Borne Sound*, 3rd edn. (Springer, Berlin, 2005)
16. M. Sato, Fundamental investigation of shear and surface elastic waves in soft biological tissues by numerical simulation. *Jpn. J. Appl. Phys.* **1** **34**(5B), 2808–2811 (1995)
17. F. Iijima, T. Tsuchiya, N. Endoh, Analysis of characteristics of underwater sound propagation in the ocean by a finite difference time domain method. *Jpn. J. Appl. Phys.* **1** **39**(5B), 3200–3204 (2000)
18. H. Suzuki, A. Omoto, K. Fujiwara, Treatment of boundary conditions by finite difference time domain method. *Acoust. Sci. Tech.* **28**, 16–26 (2007)
19. M. Toyoda, D. Takahashi, Prediction for architectural structure-borne sound by the finite-difference time-domain method. *Acoust. Sci. Tech.* **30**, 265–276 (2009)
20. M. Toyoda, H. Miyazaki, Y. Shiba, A. Tanaka, D. Takahashi, Finite-difference time-domain method for heterogeneous orthotropic media with damping. *Acoust. Sci. Tech.* **33**, 77–85 (2012)
21. L. Rayleigh, *The Theory of Sound*, vol. 2. (Cambridge University Press, Cambridge, 1877)
22. R.B. Bird, W.E. Stewart, E.N. Lightfoot. *Transport Phenomena*, 2nd edn. (Wiley, New York, 2007)
23. L.N. Liebermann, The second viscosity of liquids. *Phys. Rev.* **75**, 1415–1422 (1949)
24. H. Jiang, H. Arai, Analysis of computation error in antenna's simulation by using non-uniform mesh fdtd. *IEICE Trans. Commun.* **E83-B**, 1544–1553 (2000)
25. S. Xiao, R. Vahldieck, An improved 2D-FDTD algorithm for hybrid mode analysis of quasi-planar transmission lines, in *Proceeding of IEEE MTT-S International*, (1993). pp. 421–424

26. H. Tsuru, R. Iwatsu, Accurate numerical prediction of acoustic wave propagation. *Int. J. Adapt. Control Signal Process.* **24**, 128–141 (2010)
27. T. Asakura, S. Sakamoto, Finite-difference time-domain analysis on leak transmission characteristics of narrow gaps. *Acoust. Sci. Tech.* **32**, 182–193 (2011)
28. H.W. Chang, C.J. Randall, Finite-difference timedomain modeling of elastic wave propagation in the cylindrical coordinate system, in *Proceeding of IEEE Ultrasonics Symposium*, (1988). pp. 397–402
29. C.J. Randall, D.J. Scheibner, P.T. Wu, Multipole borehole acoustic waveforms: synthetic logs with beds and borehole washouts. *Geophysics* **56**, 1757–1769 (1991)
30. R.W. Graves, Simulating seismic wave propagation in 3D elastic media using staggered-grid finite differences. *Bull. Seismol. Soc. Am.* **86**, 1091–1106 (1996)
31. Q.H. Liu, E. Schoen, F. Daube, C. Randall, H.L. Liu, P. Lee, A three-dimensional finite difference simulation of sonic logging. *J. Acoust. Soc. Am.* **100**, 72–79 (1996)
32. R. Vossen, J.O.A. Robertsson, C.H. Chapman, Finite-difference modeling of wave propagation in a fluid-solid configuration. *Geophysics* **67**, 618–624 (2002)
33. M. Toyoda, D. Takahashi, Y. Kawai, Averaged material parameters and boundary conditions for the vibroacoustic finite-difference time-domain method with a nonuniform mesh. *Acoust. Sci. Tech.* **33**, 273–276 (2012)
34. W.C. Chew, Q.H. Liu, Perfectly matched layers for elastodynamics: a new absorbing boundary condition. *J. Comput. Acoust.* **4**, 341–359 (1996)
35. T. Uno, *Finite Difference Time Domain Method for Electromagnetic Field and Antennas* (Corona Publishing Co. Ltd, San Antonio, 1998). (in Japanese)
36. O. Schenk, K. Gartner, Solving unsymmetric sparse systems of linear equations with pardiso. *J. Future Gen. Comp. Sys.* **20**, 475–487 (2004)
37. S. Sakamoto, Phase-error analysis of high-order finite difference time domain scheme and its influence on calculation results of impulse response in closed sound field. *Acoust. Sci. Tech.* **28**(4), 295–309 (2007)

Computational Simulation in Architectural and
Environmental Acoustics

Methods and Applications of Wave-Based Computation

Sakuma, T.; Sakamoto, S.; Otsuru, T. (Eds.)

2014, XIV, 324 p. 237 illus., 38 illus. in color., Hardcover

ISBN: 978-4-431-54453-1